

Strongly coupled inert scalar sector with radiative neutrino masses

A. E. Cárcamo Hernández ^{1, 2, 3,*} Jeremy Echeverria Puentes ^{1, 2, †}
R. Pasechnik ^{4, ‡} and Daniel Salinas-Arizmendi ^{1, 2, §}

¹*Universidad Técnica Federico Santa María, Casilla 110-V, Valparaíso, Chile.*

²*Centro Científico-Tecnológico de Valparaíso, Casilla 110-V, Valparaíso, Chile.*

³*Millennium Institute for Subatomic physics at high energy frontier - SAPHIR. Fernandez Concha 700. Santiago. Chile.*

⁴*Department of Physics, Lund University, SE-223 62 Lund, Sweden.*

(Dated: October 7, 2025)

We explore the phenomenological consequences of a model with an extended scalar sector, incorporating strongly coupled inert Higgs doublets. The model introduces three Higgs doublets: one that interacts with the $SU(2)$ symmetry of the Standard Model, and two inert doublets belonging to a strongly interacting sector, embedded in the $SU(2)_2 \times SU(2)_1 \times U(1)_Y$ electroweak gauge symmetry. This symmetry structure is further supplemented by a spontaneously broken \mathbb{Z}_2 and a preserved \mathbb{Z}'_2 discrete symmetry. Our approach harnesses the exotic scalar fields emerging from this sector to implement mass-generation mechanisms. In particular, a one-loop seesaw mechanism accounts for the smallness of neutrino masses, while a universal seesaw mechanism naturally explains the hierarchy of charged fermion masses below the top quark mass. The model is shown to be consistent with current experimental constraints, including those from charged lepton flavor violation, electroweak precision observables, the Higgs diphoton decay rate, and the Higgs trilinear self-coupling. Notably, it also provides a viable interpretation of the 95 GeV diphoton excess, offering a distinctive signature of new physics beyond the Standard Model.

I. INTRODUCTION

The Standard Model (SM) is the theoretical framework that provides the most accurate description of the behavior of non-gravitational interactions. However, despite its outstanding agreement with the experimental data, challenges such as the origin of neutrino masses, the nature of dark matter and matter-antimatter asymmetry suggest the existence of new physics beyond the SM [1–4]. In addition, some fundamental considerations, such as the hierarchy problem [5–7], raise questions about the stability of the electroweak scale under quantum corrections, requiring a more robust formulation of the theoretical framework [8].

One solution to the hierarchy problem without resorting to supersymmetry is to consider the Higgs boson as a composite state, product of a new strongly coupled dynamics. In this approach the mass of the Higgs boson is saturated at energy scales not much larger than the electroweak scale [9] and generates new physical states, such as massive vector resonances [10–16] and composite scalars [17–27], which can strongly interact with the scalar sector of the SM. These interactions not only provide observable corrections to the Higgs sector, but also produce phenomena that can be experimentally tested, endowing this class of models with additional appeal. In such models, the electroweak symmetry breaking (EWSB) is product of the emergence of an effective potential at low energies of this strongly coupled sector which exhibits a non-zero vacuum expectation value (VEV) [28].

In this work, we propose a model based on an extended scalar sector including an active Higgs doublet and two inert Higgs doublets, accompanied by an extension of the electroweak gauge group to $SU(2)_2 \times SU(2)_1 \times U(1)$. In this framework, one of the $SU(2)_1$ groups is weakly coupled and contains the active Higgs doublet, while the other $SU(2)_2$ group is strongly coupled and contains the inert Higgs doublets. The model incorporates exotic scalar fields via a nonlinear sigma model in order to break the extended group symmetry, along with a symmetry breaking mechanism for a discrete symmetries $\mathbb{Z}_2 \times \mathbb{Z}'_2$. Models with two inert doublets have been extensively worked on in the literature [29–36] and inert models with strongly coupled scalar sector in [27, 37–40]. The main achievement of this work is that the design of this model allows us to take advantage of the new fields to implement a radiative neutrino mass

*Electronic address: antonio.carcamo@usm.cl

†Electronic address: jeremy.echeverria@usm.cl

‡Electronic address: roman.pasechnik@cern.ch

§Electronic address: daniel.salinas@usm.cl

generation mechanism, supplemented by a seesaw scheme to explain the mass hierarchy in the fermionic sector. In addition, we explore phenomenological constraints derived from observables such as Higgs trilinear selfcoupling, the oblique parameters S , T , and U , Higgs diphoton decay rate and processes involving leptonic flavor and lepton number violation with the possibility of baryogenesis through leptogenesis.

This model represents a natural and minimal extension of the SM, addressing in a unified way the fundamental constraints such as the fermion mass hierarchy, the smallness of neutrino masses and the hierarchy problem, while remaining compatible with current experimental constraints. Its ability to provide viable and testable predictions with projected experimental data is also analyzed.

The structure of this paper is as follows: in Sec. II we describe the model, highlighting the construction of the strongly coupled scalar sector and its relation to the mass generation mechanisms. In Sec. III we present the scalar potential and analyze the emerging particle spectrum. Sec. IV is devoted to the fermionic mass generation and hierarchy. In Section V, the constraints imposed by the trilinear Higgs self-coupling are studied. In Sec. VI we explore the parameter space compatible with the experimental constraints on the scalar sector, with emphasis in the Higgs two-photon decay. Sec. VII, VIII and IX describe the results of the analysis of the phenomenology of the fermionic sector, including lepton flavor violating processes, the feasibility of leptogenesis within this theoretical framework and the oblique parameters. In Section X, we showed that the scalar particle spectrum can account for the excess of events observed around the 95 GeV diphoton invariant mass, within a specific scenario of the model. Finally, in Sec. XI we discuss the results and present our conclusions. The full model scalar potential and the analytical expression for the effective trilinear higgs coupling are shown in Appendices A and C, respectively.

II. THE MODEL

In this section we explain the theoretical framework underpinning the proposed model, detailing its symmetry structure, particle content, and mechanisms for fermion mass generation.

The extended symmetry group, $SU(3)_C \times SU(2)_2 \times SU(2)_1 \times U(1)_Y$, introduces a strongly coupled $SU(2)_2$ sector, whereas the $SU(2)_1$ symmetry retains the electroweak symmetry of the SM. The resulting gauge group introduces effective states, such as vector resonances, whose properties are crucial for the phenomenological analyses to be discussed in subsequent sections.

To recover the EWSB of the SM, the extended symmetry group is broken to the SM group at low energies via a hierarchical spontaneous symmetry breaking (SSB) mechanism. The first stage of this breaking is triggered by a nonlinear sigma model field, Σ , transforming as the fundamental representation of the $SU(2)_2 \times SU(2)_1$ group. This field drives the transition to the SM gauge group by acquiring nonzero vacuum expectation values in its electrically neutral components [41, 42]. Additionally, the second stage of discrete SSB mechanism, related to the generation of fermion masses, is incorporated through the inclusion of a real singlet scalar field, σ . These SSB patterns are summarized schematically as follows:

$$\begin{aligned}
 & SU(3)_C \times SU(2)_2 \times SU(2)_1 \times U(1)_Y \times \mathbb{Z}_2 \times \mathbb{Z}'_2 \\
 & \quad \Downarrow v_\Sigma, v_\sigma \\
 & SU(3)_C \times SU(2)_L \times U(1)_Y \times \mathbb{Z}'_2 \\
 & \quad \Downarrow v_\phi \\
 & SU(3)_C \times U(1)_{\text{em}} \times \mathbb{Z}'_2
 \end{aligned} \tag{1}$$

where the discrete SSB mechanism is mediated by the singlet scalar field σ . In this hierarchy, the VEVs satisfy the condition $v_\Sigma \gg v_\sigma \gg v_\phi$, where v_ϕ denotes the electroweak VEV. The diagonal components of the $SU(2)_2 \times SU(2)_1$ scalar bidoublets, which are electrically neutral do acquire the VEV v_Σ .

In addition to the previously mentioned scalar singlet σ and scalar bidoublet Σ , the implementation of the seesaw mechanism for SM fermion mass generation, requires that the scalar sector also incorporates three Higgs doublets: ϕ , h_1 , and h_2 . Here, ϕ represents the SM Higgs doublet, while h_1 and h_2 are inert doublets belonging the strongly coupled dark sector since they have non trivial charges under the preserved \mathbb{Z}'_2 symmetry and transform as doublets under the $SU(2)_2$ group associated with a strongly interacting sector. The strongly coupled inert doublet h_1 and h_2 play a key role in the one-loop level radiative seesaw mechanism that yields the tiny masses of the active neutrinos. Furthermore, the gauge singlet scalar field σ is crucial to generate mixings between heavy non SM charged fermions and the SM fermions then triggering a seesaw mechanism that generates the masses of SM charged fermions lighter than the top quark. Besides that, the scalar singlet σ provides masses to the non SM heavy charged seesaw messengers.

	ϕ	h_1	h_2	σ	Σ	B_μ	$A_\mu^{(1)}$	$A_\mu^{(2)}$
$SU(3)_C$	1	1						
$SU(2)_1$	2	1	1	1	2	1	3	1
$SU(2)_2$	1	2	2	1	2	1	1	3
$U(1)_Y$	1/2	1/2	1/2	0	0	0	0	0
\mathbb{Z}_2	0	0	0	1	1	0	0	1
\mathbb{Z}'_2	0	1	1	0	0	0	0	0

Table I: Scalar and gauge assignments under the $SU(3)_C \times SU(2)_2 \times SU(2)_1 \times U(1)_Y \times \mathbb{Z}_2 \times \mathbb{Z}'_2$ symmetry.

The particle content of the gauge and scalar sectors is summarized in Table I. The $SU(2)_1$ and $SU(2)_2$ gauge bosons are denoted as $A_\mu^{(1)}$ and $A_\mu^{(2)}$, respectively. Throughout this work, the hypercharge (Y) operator is defined as follows

$$Q = T^{(3)} + Y = T_1^{(3)} + T_2^{(3)} + Y, \quad (2)$$

where T^a denotes the generator of the diagonal subgroup $SU(2)_L \subset SU(2)_1 \times SU(2)_2$, namely $T^{(a)} \equiv T_1^{(a)} + T_2^{(a)}$, with $T_1^{(a)}$ and $T_2^{(a)}$ being the generators of the $SU(2)_1$ and $SU(2)_2$ groups, respectively. The orthogonal combination of $SU(2)_1$ and $SU(2)_2$ generators is broken, giving rise to the heavy vector states.

The most general Lagrangian for this model is expressed as:

$$\mathcal{L} = \mathcal{L}_{\text{gauge}} - \mathcal{L}_{\text{fermion}} - V(\phi, h_1, h_2, \sigma, \Sigma), \quad (3)$$

where $\mathcal{L}_{\text{gauge}}$ includes the kinetic terms for the gauge bosons and scalar fields¹, as well as the effective non-linear sigma model describing the low-energy dynamics of the strongly coupled dark sector. This term governs the behavior and self-interactions of the gauge fields. The fermionic Lagrangian, $\mathcal{L}_{\text{fermion}}$, contains the interactions responsible for generating the fermion mass spectrum. Lastly, $V(\phi, h_1, h_2, \sigma, \Sigma)$ represents the scalar potential, encoding the interactions among the scalar fields.

The gauge Lagrangian, $\mathcal{L}_{\text{gauge}}$, can be written explicitly as:

$$\begin{aligned} \mathcal{L}_{\text{gauge}} = & -\frac{1}{4} \text{Tr} \left[F_{\mu\nu}^{(1)} F^{(1)\mu\nu} \right] - \frac{1}{4} \text{Tr} \left[F_{\mu\nu}^{(2)} F^{(2)\mu\nu} \right] - \frac{1}{4} B_{\mu\nu} B^{\mu\nu} + \frac{f_\Sigma^2}{2} \text{Tr} \left[(D^\mu \Sigma)^\dagger (D_\mu \Sigma) \right] \\ & + (D^\mu \phi)^\dagger (D_\mu \phi) + (D^\mu h_1)^\dagger (D_\mu h_1) + \frac{\beta^2}{2} (\phi^\dagger \phi) \text{Tr} \left[(D^\mu \Sigma)^\dagger (D_\mu \Sigma) \right] \\ & + (D^\mu h_2)^\dagger (D_\mu h_2) + \frac{1}{2} \partial_\mu \sigma \partial^\mu \sigma, \end{aligned} \quad (4)$$

where f_Σ represents the decay constant associated with the Goldstone bosons arising from the Σ field, which plays a crucial role in the dynamics of the scalar sector. The parameter β , with mass dimension, has a direct influence on the masses of the gauge bosons, however, its physical constraints are related with the underlying strong dynamics so it can be treated as a free parameter [27].

The covariant derivatives appearing in the gauge Lagrangian are defined as:

$$\begin{aligned} D_\mu \Sigma &= \partial_\mu \Sigma - ig_1 A_\mu^{(1)} \Sigma + ig_2 \Sigma A_\mu^{(2)}, \\ D_\mu \phi &= \partial_\mu \phi - ig_1 A_\mu^{(1)} \phi - i \frac{g_y}{2} B_\mu, \\ D_\mu h_n &= \partial_\mu h_n - ig_2 A_\mu^{(2)} h_n - i \frac{g_y}{2} B_\mu, \end{aligned} \quad (5)$$

where g_1 and g_2 denote the gauge couplings for the $SU(2)_1$ and $SU(2)_2$ symmetries, respectively, while g_y is the hypercharge coupling. The index $n = 1, 2$ is used to distinguish the scalar fields h_1 and h_2 , and this convention will be maintained throughout this work unless otherwise specified.

¹ The fermion kinetic terms have been omitted because they are the standard ones $i\bar{\psi}(\gamma^\mu \partial_\mu + m)\psi$.

	Q_{iL}	u_{nR}	u_{3R}	d_{iR}	T_{nL}	T_{nR}	B_{iL}	B_{iR}	L_{iL}	l_{iR}	N_R	E_{iL}	E_{iR}
$SU(3)_C$	3	1	1	1	1	1							
$SU(2)_1$	2	1	2	1	1	1	1						
$SU(2)_2$	1												
$U(1)_Y$	1/6	2/3	2/3	-1/3	2/3	2/3	-1/3	-1/3	-1	-1/2	0	-1/2	-1
\mathbb{Z}_2	0	1	0	1	0	1	0	1	0	1	0	0	1
\mathbb{Z}'_2	0	0	0	0	0	0	0	0	0	1	0	0	0

Table II: Fermionic assignments under the $SU(3)_C \times SU(2)_2 \times SU(2)_1 \times U(1)_Y \times \mathbb{Z}_2 \times \mathbb{Z}'_2$ symmetry. In this case the index $i = 1, 2, 3$; and the index $n = 1, 2$.

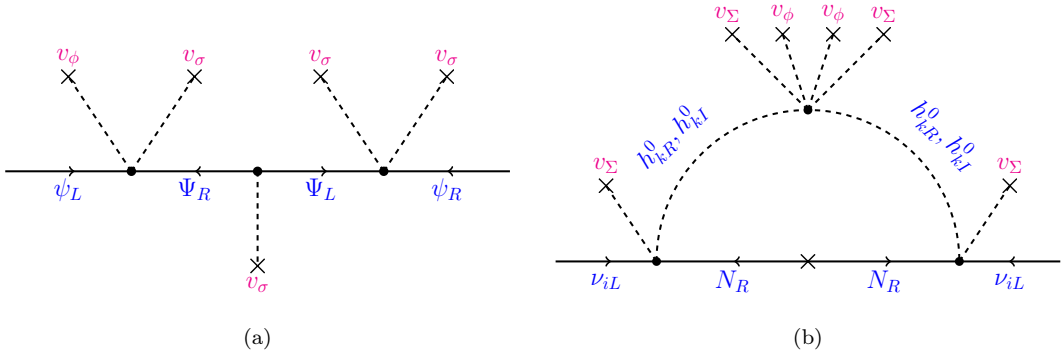


Figure 1: Fermion mass mechanism. In (a) Universal seesaw mechanism for quarks and charged lepton $\psi_L = \{Q_{nL}, e_{iL}\}$, $\psi_R = \{u_{nR}, d_{nR}, e_{iR}\}$, $\Psi_L = \{T_{nL}, B_{iL}, E_{iL}\}$ and $\Psi_R = \{T_{nR}, B_{iR}, E_{iR}\}$, for $n = 1, 2$, $i = 1, 2, 3$ (excluding top quark). In (b) One-loop radiative seesaw mechanism for neutrino sector.

In the fermionic sector, the left-handed quarks are denoted as \bar{Q}_{iL} , with $i = 1, 2, 3$ representing the family index, a convention adopted for the remainder of this study. The right-handed quarks are labeled as u_{iR} and d_{iR} for the *up*-type and *down*-type quarks, respectively.

We propose to motivate the mass generation mechanisms for the fermions of the model. First of all, the mass of the top quark will be generated at tree-level by a Yukawa interaction, as in the Standard Model:

$$\mathcal{O}_Y = \bar{Q}_{iL} \tilde{\phi} u_{3R}. \quad (6)$$

With this in mind, the particle content of the fermionic sector has been extended to include exotic fermions, singlets of $SU(2)_1 \times SU(2)_2$. Two left-handed exotic *up*-type quarks T_{nL} and three *down*-type B_{iL} have been added in conjunction with 5 right-handed T_{nR} , B_{iR} singlets. For the leptonic sector, three exotic left-handed singlets E_{iL} and three exotic right-handed singlets E_{iR} have been added.

In order to generate the masses of the other charged and exotic fermions, we will use the universal seesaw mechanism, which requires forbidding the tree-level renormalizable operators that allow the generation of masses via Yukawa interaction:

$$\bar{Q}_{iT} \tilde{\phi} u_{nR}, \quad \bar{Q}_{iT} \tilde{\phi} d_{iR}, \quad \bar{L}_L^i \tilde{\phi} l_R^i, \quad \bar{T}_{nL} \tilde{\phi} T_{nR}, \quad \bar{B}_{iT} \tilde{\phi} B_{iR}, \quad \bar{E}_{iT} \tilde{\phi} E_{iR}, \quad (7)$$

with the left-handed charged leptons given by \bar{L}_L^i and the right-handed by l_R^i . To implement this prohibition, the model is equipped with a spontaneously broken global discrete symmetry \mathbb{Z}_2 . The breaking of this discrete symmetry is due to the presence of a new real singlet scalar field, σ , charged under \mathbb{Z}_2 , which acquires a VEV. On the other hand, all right-handed fermions, excluding the top quark, are charged under \mathbb{Z}_2 .

Instead, the fermions can acquire their masses through non-renormalizable dimension-5 operators that are constructed using the SM Higgs doublet and the new singlet scalar field σ , whose form is:

$$\mathcal{O}_5 \sim \left\{ \frac{1}{\Lambda} \bar{Q}_{iL} \tilde{\phi} \sigma T_{mR}, \quad \frac{1}{\Lambda} \bar{Q}_{iL} \phi \sigma B_{jR}, \quad \frac{1}{\Lambda} \bar{L}_{iL} \phi \sigma E_{jR} \right\}. \quad (8)$$

From here, we can see the reason for the \mathbb{Z}_2 symmetry breaking: to give way to the usual Higgs mechanism at low energy. The presence of the σ field allows new renormalizable Yukawa operators:

$$\mathcal{O}_Y \sim \{\bar{T}_{nL}\sigma u_{mR}, \bar{T}_{nL}\sigma T_{mR}, \bar{B}_{iL}\sigma d_{jR}, \bar{B}_{iL}\sigma B_{jR}, \bar{E}_{iL}\sigma l_{jR}, \bar{E}_{iL}\sigma E_{jR}\}, \quad (9)$$

these together form a universal seesaw mechanism to provide mass to all fermions.

Regarding the neutrino sector, a one-loop level radiative seesaw mechanism will be used in order to generate the tiny masses for the active neutrinos. This implies that the smallness of active neutrino masses will be attributed to the loop suppression as well as to the small mass splitting between the physical dark scalars and dark pseudoscalars. The successfull implementation of such radiative seesaw mechanism requires the inclusion of a right-handed sterile heavy Majorana neutrino N_R as well as a preserved discrete symmetry \mathbb{Z}'_2 . This unbroken \mathbb{Z}'_2 symmetry is crucial to forbid tree-level masses for active neutrinos at all energy scales. To build the loop, we will use the inert Higgs doublets h_1 and h_2 in combination with the scalar bidoublet Σ to construct the non-renormalizable operators:

$$\mathcal{O}_\nu \sim \left\{ \frac{1}{\Lambda} \bar{L}_{iL} \tilde{h}_1 \Sigma N_R, \frac{1}{\Lambda} \bar{L}_{iL} \tilde{h}_2 \Sigma N_R \right\}, \quad (10)$$

and forbid others by making h_1 , h_2 and N_R charged under the preserved \mathbb{Z}'_2 symmetry. Such loop will be closed by the following non renormalizable scalar interactions:

$$\mathcal{O}_s \sim \left\{ \frac{1}{\Lambda^2} (\phi^\dagger \Sigma h_1)^2, \frac{1}{\Lambda^2} (\phi^\dagger \Sigma h_2)^2 \right\}, \quad (11)$$

that will generate a small mass splitting between the dark CP even and dark CP odd scalars running in the internal lines of the neutrino loop diagram.

In conclusion, in this model, the masses of fermions are generated by a combination of a tree level universal seesaw mechanism for SM charged fermions lighter than the top quark and a radiative seesaw mechanism for active neutrinos, as we shown in Figure 1, which follows from the particle field assignments under the symmetries of the model displayed in Table II.

Finally, with the particle content and symmetries specified in Table II, the following Yukawa interactions arise:

$$\begin{aligned} \mathcal{L}_{\text{fermion}} = & \sum_i Y_i^1 \bar{Q}_{iL} \tilde{\phi} u_{3R} + \sum_{i,m} \frac{Y_{im}^2}{\Lambda} \bar{Q}_{iL} \tilde{\phi} \sigma T_{mR} + \sum_{n,m} Y_{nm}^3 \bar{T}_{nL} \sigma u_{mR} + \sum_{n,m} Y_{nm}^4 \bar{T}_{nL} \sigma T_{mR} \\ & + \sum_{i,j} \frac{Y_{ij}^5}{\Lambda} \bar{Q}_{iL} \phi \sigma B_{jR} + \sum_{i,j} Y_{ij}^6 \bar{B}_{iL} \sigma d_{jR} + \sum_{i,j} Y_{ij}^7 \bar{B}_{iL} \sigma B_{jR} + \sum_{i,j} y_{ij}^1 \bar{E}_{iL} \sigma l_{jR} \\ & + \sum_{i,j} y_{ij}^2 \bar{E}_{iL} \sigma E_{jR} + \sum_{i,j} \frac{y_{ij}^3}{\Lambda} \bar{L}_{iL} \phi \sigma E_{jR} + \sum_i \frac{y_i^4}{\Lambda} \bar{L}_{iL} \tilde{h}_1 \Sigma N_R + \sum_i \frac{y_i^5}{\Lambda} \bar{L}_{iL} \tilde{h}_2 \Sigma N_R + m_N N_R \bar{N}_R^c + H.c. \end{aligned} \quad (12)$$

where $i, j = 1, 2, 3$, $m, n = 1, 2$ and the model cutoff Λ is the scale of the UV completion of the model.

III. SCALAR POTENTIAL AND SCALAR MASS SPECTRUM

In this section, we will analyze the low-energy scalar potential of the model. The most general scalar potential invariant under the symmetry in Eq. (1) (see Table I) reads:

$$\begin{aligned} V = & \mu_\phi^2 (\phi \phi^\dagger) + \mu_{h_1}^2 (h_1 h_1^\dagger) + \mu_{h_2}^2 (h_2 h_2^\dagger) + \mu_{h_{12}}^2 (h_1 h_2^\dagger + \text{H.c.}) + \mu_\Sigma^2 \text{Tr} (\Sigma \Sigma^\dagger) + \mu_{\Sigma'}^2 \text{Tr} [\Sigma^2 + (\Sigma^*)^2] \\ & + \mu_\sigma^2 (\sigma \sigma) + \lambda_1 (\phi \phi^\dagger) (\phi \phi^\dagger) + \lambda_2 (\phi \phi^\dagger) (h_1 h_1^\dagger) + \lambda_3 (\phi \phi^\dagger) (h_2 h_2^\dagger) + \lambda_4 (\phi \phi^\dagger) (h_1 h_2^\dagger + \text{H.c.}) \\ & + \lambda_5 (\phi \phi^\dagger) \text{Tr} (\Sigma \Sigma^\dagger) + \lambda_6 (\phi \phi^\dagger) (\sigma \sigma) + \lambda_7 (h_1 h_1^\dagger) (h_1 h_1^\dagger) + \lambda_8 (h_1 h_1^\dagger) (h_2 h_2^\dagger) + \frac{1}{2} \left[\lambda_9 (h_1 h_2^\dagger)^2 + \text{H.c.} \right] \\ & + \lambda_{10} (h_1 h_1^\dagger) (h_1 h_2^\dagger + \text{H.c.}) + \lambda_{11} (h_1 h_1^\dagger) \text{Tr} (\Sigma \Sigma^\dagger) + \lambda_{12} (h_1 h_1^\dagger) (\sigma \sigma) + \lambda_{13} (h_2 h_2^\dagger) (h_2 h_2^\dagger) \\ & + \lambda_{14} (h_2 h_2^\dagger) (h_1 h_2^\dagger + \text{H.c.}) + \lambda_{15} (h_2 h_2^\dagger) \text{Tr} (\Sigma \Sigma^\dagger) + \lambda_{16} (h_2 h_2^\dagger) (\sigma \sigma) + \lambda_{17} (h_1 h_2^\dagger + \text{H.c.}) \text{Tr} (\Sigma \Sigma^\dagger) \\ & + \lambda_{18} (h_1 h_2^\dagger + \text{H.c.}) (\sigma \sigma) + \lambda_{19} \text{Tr} (\Sigma \Sigma^\dagger) \text{Tr} (\Sigma \Sigma^\dagger) + \lambda_{20} \text{Tr} [(\Sigma \Sigma^\dagger)^2] + \lambda_{21} \text{Tr} (\Sigma \Sigma^\dagger) (\sigma \sigma) \\ & + \lambda_{22} (\sigma \sigma) (\sigma \sigma) + \lambda_{23} \text{Tr} (\tilde{\Sigma}^\dagger \tilde{\Sigma}) \text{Tr} (\tilde{\Sigma}^\dagger \tilde{\Sigma}) + \lambda_{24} \text{Tr} [(\tilde{\Sigma}^\dagger \tilde{\Sigma})^2] + \lambda_{25} (\phi \phi^\dagger) \text{Tr} (\tilde{\Sigma} \tilde{\Sigma}^\dagger) + \lambda_{26} (h_1 h_1^\dagger) \text{Tr} (\tilde{\Sigma} \tilde{\Sigma}^\dagger) \end{aligned} \quad (13)$$

$$\begin{aligned}
& + \lambda_{27} \left(h_2 h_2^\dagger \right) \text{Tr} \left(\tilde{\Sigma} \tilde{\Sigma}^\dagger \right) + \lambda_{28} \left(h_1 h_2^\dagger + \text{H.c.} \right) \text{Tr} \left(\tilde{\Sigma} \tilde{\Sigma}^\dagger \right) + \lambda_{29} \text{Tr} \left(\tilde{\Sigma} \tilde{\Sigma}^\dagger \right) (\sigma \sigma) + \lambda_{30} \text{Tr} \left[\Sigma^2 + (\Sigma^*)^2 \right]^2 \\
& + \lambda_{31} (\phi \phi^\dagger) \text{Tr} \left[\Sigma^2 + (\Sigma^*)^2 \right] + \lambda_{32} \left(h_1 h_1^\dagger \right) \text{Tr} \left[\Sigma^2 + (\Sigma^*)^2 \right] + \lambda_{33} \left(h_2 h_2^\dagger \right) \text{Tr} \left[\Sigma^2 + (\Sigma^*)^2 \right] \\
& + \lambda_{34} \left(h_1 h_2^\dagger + \text{H.c.} \right) \text{Tr} \left[\Sigma^2 + (\Sigma^*)^2 \right] + \lambda_{35} \text{Tr} \left[\Sigma^2 + (\Sigma^*)^2 \right] (\sigma \sigma) + \lambda_{36} \text{Tr} \left(\Sigma \Sigma^\dagger \right) \text{Tr} \left[\Sigma^2 + (\Sigma^*)^2 \right] \\
& + \lambda_{37} \text{Tr} \left(\tilde{\Sigma} \tilde{\Sigma}^\dagger \right) \text{Tr} \left[\Sigma^2 + (\Sigma^*)^2 \right] + \lambda_{38} \text{Tr} \left[(\Sigma^2 + (\Sigma^*)^2)^2 \right] + \frac{\alpha_1}{\Lambda^2} |\phi^\dagger \Sigma h_1|^2 + \frac{\alpha_2}{\Lambda^2} |\phi^\dagger \Sigma h_2|^2 \\
& + \frac{\alpha_3}{\Lambda^2} \left[(\phi^\dagger \Sigma h_1)^2 + (h_1^\dagger \Sigma^\dagger \phi)^2 \right] + \frac{\alpha_4}{\Lambda^2} \left[(\phi^\dagger \Sigma h_2)^2 + (h_2^\dagger \Sigma^\dagger \phi)^2 \right] + \frac{\alpha_5}{\Lambda^2} |\phi^\dagger \tilde{\Sigma} h_1|^2 + \frac{\alpha_6}{\Lambda^2} |\phi^\dagger \tilde{\Sigma} h_2|^2 \\
& + \frac{\alpha_7}{\Lambda^2} \left[(\phi^\dagger \tilde{\Sigma} h_1)^2 + (h_1^\dagger \tilde{\Sigma}^\dagger \phi)^2 \right] + \frac{\alpha_8}{\Lambda^2} \left[(\phi^\dagger \tilde{\Sigma} h_2)^2 + (h_2^\dagger \tilde{\Sigma}^\dagger \phi)^2 \right].
\end{aligned}$$

Here, $\mu_{\phi, h_{1,2}, \Sigma, \sigma}$ are the dimensionfull parameters of the SM Higgs doublet, the inert Higgs doublets, the scalar bi-doublet, and the scalar singlet, respectively; λ_i are the dimensionless quartic couplings, and α_i are the dimensionless couplings of dimension-6 operators necessary for closing the loop in Figure 1. The full scalar potential, including operators up to dimension-6, can be found in Appendix A.

The scalar fields of the model can be expanded as:

$$\begin{aligned}
\phi &= \frac{1}{\sqrt{2}} \begin{pmatrix} \sqrt{2} \phi^+ \\ v_\phi + \phi_R^0 + i\phi_I^0 \end{pmatrix}, \quad \Sigma = \frac{1}{\sqrt{2}} \begin{pmatrix} v_\Sigma + \Sigma_{1R}^0 + i\Sigma_{1I}^0 & \sqrt{2} \Sigma_2^+ \\ \sqrt{2} \Sigma_1^- & v_\Sigma + \Sigma_{2R}^0 + i\Sigma_{2I}^0 \end{pmatrix}, \\
h_k &= \frac{1}{\sqrt{2}} \begin{pmatrix} \sqrt{2} h_k^+ \\ h_{kR}^0 + i h_{kI}^0 \end{pmatrix}, \quad \sigma = v_\sigma + \tilde{\sigma}, \quad k = 1, 2.
\end{aligned} \tag{14}$$

where v_ϕ is the VEV responsible for the EWSB.

A. Gauge sector

The masses of the electroweak gauge bosons arise from the gauge part of the Lagrangian in Eq.(4) after the high-energy symmetry breaking. Using the field parametrization of the Σ field in Eq.(14), the Lagrangian takes the form:

$$\begin{aligned}
\mathcal{L}_{\text{gauge}} = & -\frac{1}{4} \text{Tr} \left[F_{\mu\nu}^{(1)} F^{(1)\mu\nu} \right] - \frac{1}{4} \text{Tr} \left[F_{\mu\nu}^{(2)} F^{(2)\mu\nu} \right] - \frac{1}{4} B_{\mu\nu} B^{\mu\nu} + f_\Sigma^2 v_\Sigma^2 (\phi^\dagger \phi) \left(-ig_1 A_\mu^{(1)} + ig_2 A_\mu^{(2)} \right)^2 \\
& + (D^\mu \phi)^\dagger (D_\mu \phi) + (D^\mu h_1)^\dagger (D_\mu h_1) + (D^\mu h_2)^\dagger (D_\mu h_2) + \beta^2 v_\Sigma^2 (\phi^\dagger \phi) \left(-ig_1 A_\mu^{(1)} + ig_2 A_\mu^{(2)} \right)^2,
\end{aligned} \tag{15}$$

on the other hand, the EWSB will occur when ϕ acquires its VEV. Gauge bosons will be parametrized as usual:

$$A_\pm^{(1/2)} = \frac{1}{\sqrt{2}} \left(A_1^{(1/2)} \mp A_2^{(1/2)} \right). \tag{16}$$

After the SSB processes, the squared neutral mass matrix for the gauge fields in the $(B_\mu, A_3^{(1)}, A_3^{(2)})$ basis is:

$$M_N^2 = \frac{v_\phi^2}{4} \begin{pmatrix} g_y^2 & -g_1 g_y & 0 \\ -g_1 g_y & (1+c^2) g_1^2 & -c^2 g_1 g_2 \\ 0 & -c^2 g_1 g_2 & c^2 g_2^2 \end{pmatrix}, \tag{17}$$

and the charged matrix in the $(A_\pm^{(1)}, A_\pm^{(2)})$ basis:

$$M_{CH}^2 = \frac{v_\phi^2}{4} \begin{pmatrix} (1+c^2) g_1^2 & -c^2 g_1 g_2 \\ -c^2 g_1 g_2 & c^2 g_2^2 \end{pmatrix}. \tag{18}$$

The parameters a , b , and c are defined as:

$$a = f_\Sigma \frac{v_\Sigma}{v_\phi}, \quad b = \beta \frac{v_\Sigma}{\sqrt{2}} \quad \text{and} \quad c^2 = a^2 + b^2. \tag{19}$$

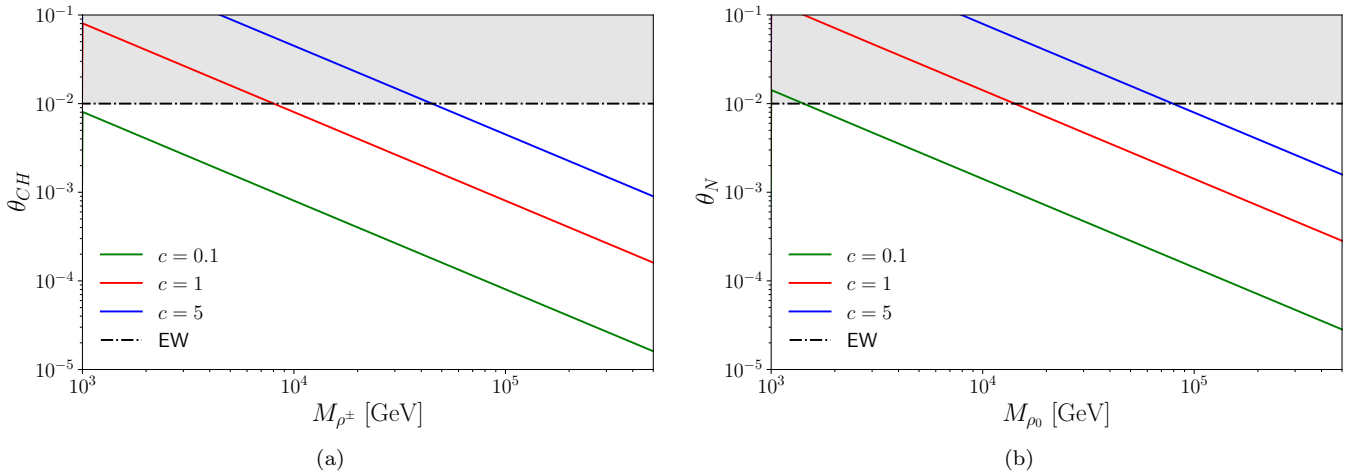


Figure 2: Panel (a): Behavior of the mixing angle θ_{CH} as a function of the charged vector resonance mass M_{ρ^\pm} for different values of the c parameter. The horizontal black dashed-dotted line indicates the exclusion region arising from the electroweak precision data and is denoted as “EW” [44]. Panel (b): Behavior of the mixing angle θ_N as a function of the neutral vector resonance mass M_{ρ_0} for different values of the c parameter. The horizontal black dashed-dotted line indicates the exclusion region resulting from the electroweak precision data (EW) [44].

The physical eigenstates can be defined by [27]:

$$\begin{pmatrix} A_\mu \\ Z_\mu \\ \rho_\mu^0 \end{pmatrix} = \begin{pmatrix} \cos \theta_W & \sin \theta_W & 0 \\ -\cos \theta_N \sin \theta_W & \cos \theta_N \cos \theta_W & -\sin \theta_N \\ -\sin \theta_N \sin \theta_W & \cos \theta_W \sin \theta_N & \cos \theta_N \end{pmatrix} \begin{pmatrix} B_\mu \\ A_{\mu,3}^{(1)} \\ A_{\mu,3}^{(2)} \end{pmatrix} \quad (20)$$

where θ_W is the electroweak mixing angle, $\tan \theta_W = g_y/g_1$, and the mixing angle from the strong sector θ_N is given by:

$$\tan 2\theta_N = -\frac{2c^2 g_1^2 g_2}{(1+c^2)g_1^3 + g_1 g_y^2 - c^2 g_2^2 \sqrt{g_1^2 + g_y^2}}, \quad (21)$$

and

$$\begin{pmatrix} W_\mu^\pm \\ \rho_\mu^\pm \end{pmatrix} = \begin{pmatrix} \cos \theta_{CH} & -\sin \theta_{CH} \\ \sin \theta_{CH} & \cos \theta_{CH} \end{pmatrix} \begin{pmatrix} A_{\mu,\pm}^{(1)} \\ A_{\mu,\pm}^{(2)} \end{pmatrix}. \quad (22)$$

The combination with extra $SU(2)_2$ gauge fields gives rise to new physical states in the form of two strong vector resonances ρ_μ^0 and ρ_μ^\pm . The mixing angle θ_{CH} is given by:

$$\tan 2\theta_{CH} = -\frac{2c^2 g_1 g_2}{(1+c^2)g_1^2 - c^2 g_2^2}. \quad (23)$$

The mixing angles of exotic electroweak bosons have been strongly constrained in the literature, for instance in [43, 44]. Our numerical analysis shows that the mass of the vector resonances lies above the exclusion limits set by ATLAS and CMS Run 2 data [44]. In Fig. 2 the behavior of the mixing angles as a function of the masses of the exotic vector resonances is shown for different values of the c parameter. Allowed values consistent with electroweak precision data are achieved for large vector resonance masses provided that the c parameter is large. The predictions of this model for lighter mass resonances and their mixings with the Standard Model can be studied in detail in future works.

If M_N^2 and M_{CH}^2 are diagonalized in the limit $g_2 \gg g_1$ the following masses for the gauge bosons and strong vector

resonances are obtained

$$\begin{aligned}
M_A^2 &= 0 \quad (\text{exact}), \\
M_Z^2 &= \frac{v_\phi^2}{4}(g_1^2 + g_y^2) + \mathcal{O}((g_1/g_2)^2), \\
M_{\rho_0}^2 &= \frac{v_\phi^2}{4}c^2g_2^2 + \mathcal{O}((g_1/g_2)^2), \\
M_{W^\pm}^2 &= \frac{v_\phi^2}{4}g_1^2 + \mathcal{O}((g_1/g_2)^2), \\
M_{\rho^\pm}^2 &= \frac{v_\phi^2}{4}c^2g_2^2 + \mathcal{O}((g_1/g_2)^2).
\end{aligned} \tag{24}$$

Full expressions for the masses are given in Appendix B.

B. Scalar sector

We are going to start applying the conditions that it has given rise to the SSB processes, we impose that the gradient of the scalar potential vanishes when the neutral components of ϕ , Σ and σ acquire a v_ϕ , v_Σ and v_σ VEV respectively. The dimension 6 operators are not considered because it is only relevant for high energies. The conditions impose the following restrictions on the μ -parameters:

$$\mu_\phi^2 = -\lambda_1 v_\phi^2 - (\lambda_5 + \lambda_{25} + 2\lambda_{35})v_\Sigma^2 - \lambda_6 v_\sigma^2, \tag{25}$$

$$\begin{aligned}
\mu_\Sigma^2 &= -\frac{1}{2}(\lambda_5 + \lambda_{25} + 2\lambda_{31})v_\phi^2 - (2\lambda_{19} + \lambda_{20} + 2\lambda_{23} + \lambda_{24} + 4(2\lambda_{30} + \lambda_{36} + \lambda_{37} + \lambda_{38}))v_\Sigma^2 \\
&\quad - (\lambda_{21} + \lambda_{29} + 2\lambda_{35})v_\sigma^2 - 4\mu_{\Sigma'}^2,
\end{aligned} \tag{26}$$

$$\mu_\sigma^2 = -\frac{1}{2}v_\phi^2\lambda_6 - 2\lambda_{22}v_\sigma^2 - (\lambda_{21} + \lambda_{29} + 2\lambda_{35})v_\Sigma^2. \tag{27}$$

The next step is to ensure the tree-level stability of the potential, *i.e.* to impose restrictions on the potential couplings as long as the potential is bounded from below. Using the following definitions for the bilinear combination of scalar fields:

$$\begin{aligned}
A &= \phi^\dagger\phi, & B &= h_1^\dagger h_1, & C &= h_2^\dagger h_2, & D &= \text{Tr}[\Sigma^\dagger\Sigma], \\
E &= \sigma^2, & F &= \text{Re}[h_1^\dagger h_2], & G &= \text{Im}[h_1^\dagger h_2], & H^2 &= \text{Tr}[(\Sigma^\dagger\Sigma)^2].
\end{aligned} \tag{28}$$

we can rewrite the quartic part of the potential as²:

$$\begin{aligned}
V_4 &= \left(\sqrt{\lambda_1}A - \sqrt{\lambda_7}B\right)^2 + \left(\sqrt{\lambda_1}A - \sqrt{\lambda_{13}}C\right)^2 + \left(\sqrt{\lambda_1}A - \sqrt{\lambda_{19}}D\right)^2 + \left(\sqrt{\lambda_1}A - \sqrt{\lambda_{22}}E\right)^2 \\
&\quad + \left(\sqrt{\lambda_7}B - \sqrt{\lambda_{13}}C\right)^2 + \left(\sqrt{\lambda_7}B - \sqrt{\lambda_{19}}D\right)^2 + \left(\sqrt{\lambda_7}B - \sqrt{\lambda_{22}}E\right)^2 + \left(\sqrt{\lambda_{13}}C - \sqrt{\lambda_{19}}D\right)^2 \\
&\quad + \left(\sqrt{\lambda_{13}}C - \sqrt{\lambda_{22}}E\right)^2 + \left(\sqrt{\lambda_{19}}D - \sqrt{\lambda_{22}}E\right)^2 + 4(\lambda_8 + 2\sqrt{\lambda_7}\sqrt{\lambda_{13}})F^2 + \lambda_{22}H^2 \\
&\quad + 2(\lambda_2 + 2\sqrt{\lambda_1}\sqrt{\lambda_7})AB + 2(\lambda_3 + 2\sqrt{\lambda_1}\sqrt{\lambda_{13}})AC + 2(\lambda_5 + 2\sqrt{\lambda_1}\sqrt{\lambda_{19}})AD + 2(\lambda_6 + 2\sqrt{\lambda_1}\sqrt{\lambda_{22}})AE \\
&\quad + 2(\lambda_8 + 2(\lambda_{11} + 2\sqrt{\lambda_7}\sqrt{\lambda_{19}})BD + 2\sqrt{\lambda_7}\sqrt{\lambda_{13}})(BC - F^2 - G^2) + 2(\lambda_{12} + 2\sqrt{\lambda_7}\sqrt{\lambda_{22}})BE \\
&\quad + 2(\lambda_{15} + 2\sqrt{\lambda_{13}}\sqrt{\lambda_{19}})CD + 2(\lambda_{16} + 2\sqrt{\lambda_{13}}\sqrt{\lambda_{22}})CE + 2(\lambda_{21} + 2\sqrt{\lambda_{19}}\sqrt{\lambda_{22}})DE - 2\text{Im}(\lambda_9)FG \\
&\quad + (\text{Re}(\lambda_9) - 2\lambda_8 - 4\sqrt{\lambda_7}\sqrt{\lambda_{13}})(F^2 - G^2) + 2\lambda_4AF + \lambda_{10}BF + \lambda_{14}CF + \lambda_{17}DF + \lambda_{18}EF,
\end{aligned} \tag{29}$$

² The terms involving $\tilde{\Sigma}$ have been omitted since their behavior is identical to that of Σ .

Using the method presented in [45] we obtain the following restrictions for the couplings of the scalar potential:

$$\begin{aligned}
& \lambda_1, \lambda_4, \lambda_7, \lambda_{10}, \lambda_{13}, \lambda_{14}, \lambda_{17}, \lambda_{18}, \lambda_{19}, \lambda_{20}, \lambda_{22}, \lambda_{23}, \lambda_{24}, \lambda_{28}, \lambda_{30}, \lambda_{34}, \lambda_{38} \geq 0, \\
& \lambda_2 + 2\sqrt{\lambda_1}\sqrt{\lambda_7} \geq 0, \quad \lambda_3 + 2\sqrt{\lambda_1}\sqrt{\lambda_{13}} \geq 0, \quad \lambda_5 + 2\sqrt{\lambda_1}\sqrt{\lambda_{19}} \geq 0, \quad \lambda_{25} + 2\sqrt{\lambda_1}\sqrt{\lambda_{23}} \geq 0, \\
& \lambda_6 + 2\sqrt{\lambda_1}\sqrt{\lambda_{22}} \geq 0, \quad \lambda_8 + 2\sqrt{\lambda_{13}}\sqrt{\lambda_7} \geq 0, \quad \lambda_{11} + 2\sqrt{\lambda_{19}}\sqrt{\lambda_7} \geq 0, \quad \lambda_{26} + 2\sqrt{\lambda_{23}}\sqrt{\lambda_7} \geq 0, \\
& \lambda_{12} + 2\sqrt{\lambda_{22}}\sqrt{\lambda_7} \geq 0, \quad \lambda_{15} + 2\sqrt{\lambda_{13}}\sqrt{\lambda_{19}} \geq 0, \quad \lambda_{27} + 2\sqrt{\lambda_{13}}\sqrt{\lambda_{23}} \geq 0, \quad \lambda_{25} + 2\sqrt{\lambda_1}\sqrt{\lambda_{23}} \geq 0, \\
& \lambda_{31} + 2\sqrt{\lambda_1}\sqrt{\lambda_{30}} \geq 0, \quad \lambda_{32} + 2\sqrt{\lambda_7}\sqrt{\lambda_{30}} \geq 0, \quad \lambda_{33} + 2\sqrt{\lambda_8}\sqrt{\lambda_{30}} \geq 0, \quad \lambda_{16} + 2\sqrt{\lambda_{13}}\sqrt{\lambda_{22}} \geq 0, \\
& \lambda_{21} + 2\sqrt{\lambda_{19}}\sqrt{\lambda_{22}} \geq 0, \quad |\lambda_9| < 2\lambda_8 + 4\sqrt{\lambda_7}\sqrt{\lambda_{13}}.
\end{aligned} \tag{30}$$

Applying the conditions of Eq.(27) we can obtain the mass matrices with respect to the components of the scalar fields. The sector formed by the components of the inert scalar fields, or dark sector, is separated from the sector formed by the active fields, or visible sector.

The squared mass matrices for the neutral CP-even visible scalar fields that transform trivially under the preserved $\mathbb{Z}_2 \times \mathbb{Z}'_2$ symmetry in the basis $(\phi_R^0, \Sigma_{1R}^0, \Sigma_{2R}^0, \tilde{\sigma})$ are given by:

$$M_{\text{CP-even}}^2 = \begin{pmatrix} v_\phi^2 \lambda_1 & \lambda_B & \lambda_B & v_\sigma v_\phi \lambda_6 \\ \lambda_B & \lambda_A & \lambda_C & \lambda_D \\ \lambda_B & \lambda_C & \lambda_A & \lambda_D \\ v_\sigma v_\phi \lambda_6 & \lambda_D & \lambda_D & 4v_\sigma^2 \lambda_{22} \end{pmatrix}, \tag{31}$$

where:

$$\begin{aligned}
\lambda_A &= v_\Sigma^2 (\lambda_{19} + \lambda_{20} + \lambda_{23} + \lambda_{24} + 4\lambda_{30} + 2\lambda_{36} + 2\lambda_{37} + 4\lambda_{38}) \\
\lambda_B &= \frac{1}{2} v_\Sigma v_\phi (\lambda_{25} + 2\lambda_{31} + \lambda_5) \\
\lambda_C &= v_\Sigma^2 (\lambda_{19} + \lambda_{23} + 2(2\lambda_{30} + \lambda_{36} + \lambda_{37})) \\
\lambda_D &= v_\sigma v_\Sigma (\lambda_{21} + \lambda_{29} + 2\lambda_{35}),
\end{aligned} \tag{32}$$

and which has four distinct eigenvalues. The lightest eigenstate is identified as the 126 GeV SM-like Higgs boson, h , while the other three massive states correspond to physical fields which we name Σ_1 , Σ_2 , and H_3^0 . Symbolic expression for the masses are very extensive to be included in this section, so we will simply work with their numerical values.

The squared mass matrix for the neutral CP-odd visible scalar fields in the basis $(\phi_I^0, \Sigma_{1I}^0, \Sigma_{2I}^0)$ is given by:

$$M_{\text{CP-odd}}^2 = \begin{pmatrix} 0 & 0 & 0 \\ 0 & \lambda_E & 0 \\ 0 & 0 & \lambda_E \end{pmatrix}, \tag{33}$$

where

$$\lambda_E = -v_\phi^2 \lambda_{31} - 2v_\Sigma^2 (4\lambda_{30} + \lambda_{36} + \lambda_{37} + 2\lambda_{38}) - 2(v_\sigma^2 \lambda_{35} + \mu_{\Sigma'}^2). \tag{34}$$

The massless state correspond to the Goldstone bosons associated with the breaking of gauge symmetry. One of these corresponds to the G_0 of the SM, which is the longitudinal component of the SM Z -boson. The non-zero eigenvalues corresponds to a CP-odd scalars $\xi_{1,2}$.

The mass matrix for the charged visible scalar fields in the basis $(\phi^\pm, \Sigma_1^\pm, \Sigma_2^\pm)$ is given by:

$$M_{\text{charged}}^2 = \begin{pmatrix} 0 & 0 & 0 \\ 0 & \lambda_E & -\lambda_E \\ 0 & -\lambda_E & \lambda_E \end{pmatrix}, \tag{35}$$

which contains two Nambu–Goldstone bosons, G_\pm , that provide the longitudinal polarizations of the W_\pm bosons, and one massive charged state, η_2^\pm .

In addition, a massless charged scalar state arises due to the symmetry of the matrix of Eq.(35). This symmetry, however, is broken by quantum corrections, leading to a nonzero mass for η_1^\pm at the one-loop level. The one-loop

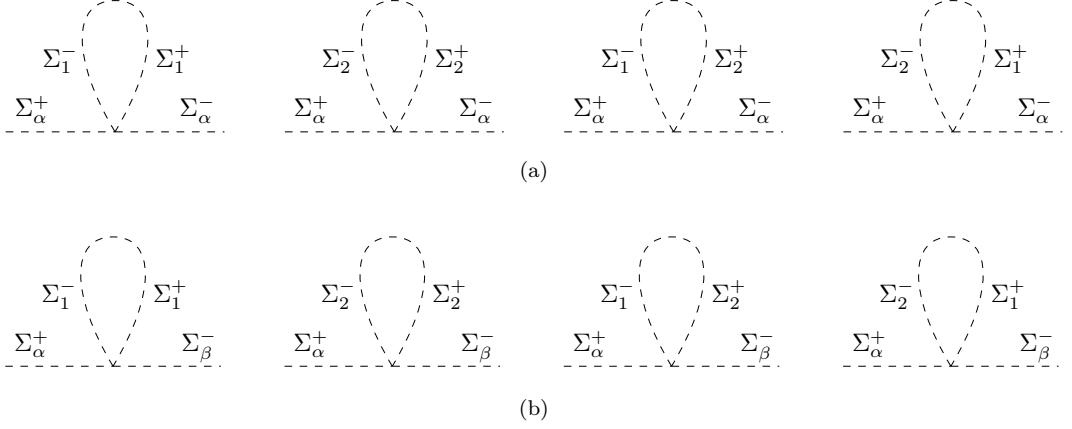


Figure 3: One-loop Feynman diagrams that contribute to the mass of the visible charged scalars. (a) Diagrams contributing to the diagonal entries of the mass matrix. Here $\alpha = 1, 2$. (b) Diagrams contributing to the off-diagonal entries of the mass matrix. Here $\alpha, \beta = 1, 2$ and $\alpha \neq \beta$.

corrected mass matrix is given by:

$$M_{\text{charged}}^{(1\text{-loop})^2} = \begin{pmatrix} 0 & 0 & 0 \\ 0 & \lambda_E + \Delta(\mu) & -\lambda_E + \Delta'(\mu) \\ 0 & -\lambda_E + \Delta'(\mu) & \lambda_E + \Delta(\mu) \end{pmatrix}, \quad (36)$$

where $\Delta(\mu)$ and $\Delta'(\mu)$ are the radiative corrections arising from the Feynman diagrams of Figure 3, evaluated in the $\overline{\text{MS}}$ scheme:

$$\begin{aligned} \Delta(\mu) &= \frac{\lambda_E}{16\pi^2} \left[(\gamma_1 + \gamma_2) - (\gamma_1 + \gamma_2 - 2\gamma_3) \ln \frac{\lambda_E}{\mu^2} \right], \\ \Delta'(\mu) &= \frac{\lambda_E}{16\pi^2} \left[2\gamma_3 - (2\gamma_3 - \gamma_2 - \gamma_4) \ln \frac{\lambda_E}{\mu^2} \right], \end{aligned} \quad (37)$$

with the coefficients defined as

$$\begin{aligned} \gamma_1 &= 4(\lambda_{19} + \lambda_{20} + \lambda_{23} + \lambda_{34}), \\ \gamma_2 &= 2(\lambda_{19} + \lambda_{23} + 4\lambda_{30} + 2\lambda_{38}), \\ \gamma_3 &= 4(\lambda_{36} + \lambda_{37}), \\ \gamma_4 &= 8(2\lambda_{30} + \lambda_{38}), \end{aligned} \quad (38)$$

where all quartic couplings originate from the Feynman diagrams shown in Figure 3. These corrections visibly break the symmetry of the tree-level mass matrix, as the contributions to the off-diagonal elements differ from those ones associated to the diagonal ones.

Using the coupling values from our benchmark point, we extract the numerical values of the charged scalar masses. As shown in Figure 4, the one loop induced mass of η_1^\pm is sufficiently large to lie beyond the current collider sensitivity for charged scalars [46]. In contrast, the quantum corrections to η_2^\pm are small, resulting in a mass that remains nearly identical to its tree-level value.

For the dark sector, it is unnecessary to analyze particles individually because the mass matrices are degenerate and can be expressed as:

$$\widetilde{M}^2 = \frac{1}{4} \begin{pmatrix} \Delta_A & \Delta_B \\ \Delta_B & \Delta_C \end{pmatrix}, \quad (39)$$

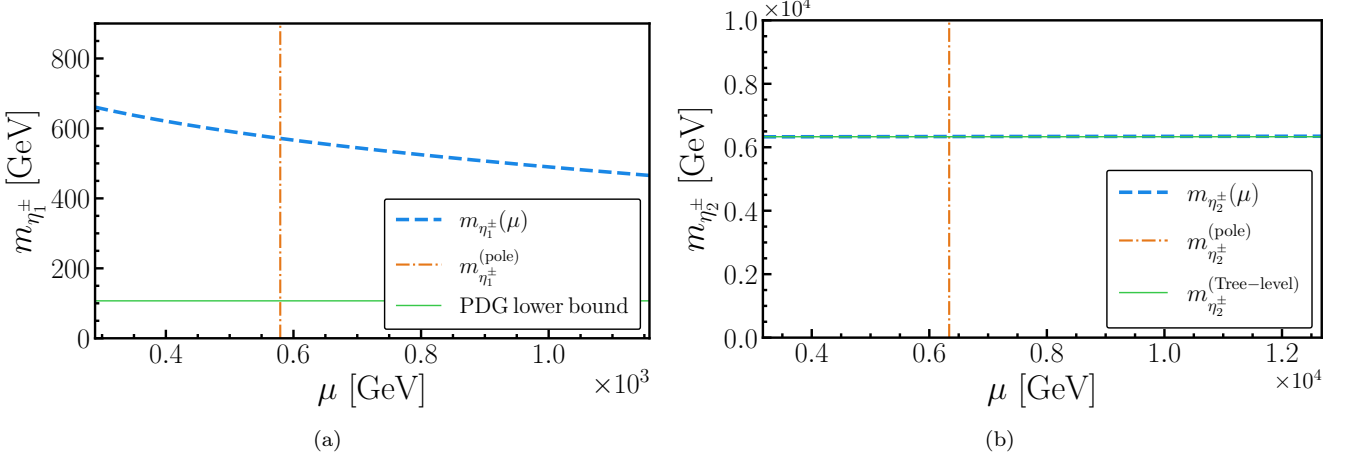


Figure 4: The one-loop running of the charged scalar masses around the pole mass is shown. Panel (a) displays the running of $m_{\eta_1^\pm}$ in the range $\left[0.5m_{\eta_1^\pm}^{(\text{pole})}, 2m_{\eta_1^\pm}^{(\text{pole})}\right]$ and the lower bound for collider searches [46]. Panel (b) presents the running of $m_{\eta_2^\pm}$ in the range $\left[0.5m_{\eta_2^\pm}^{(\text{pole})}, 2m_{\eta_2^\pm}^{(\text{pole})}\right]$, compared to its tree-level value.

where the parameters are defined as:

$$\Delta_A = v_\sigma^2 \lambda_{12} + \frac{1}{2} v_\phi^2 \lambda_2 + v_\Sigma^2 (\lambda_{11} + \lambda_{26} + 2\lambda_{32}) + \mu_{h_1}^2, \quad (40)$$

$$\Delta_B = v_\sigma^2 \lambda_{18} + v_\Sigma^2 (\lambda_{17} + \lambda_{28} + 2\lambda_{34}) + \frac{1}{2} v_\phi^2 \lambda_4 + \mu_{h_{12}}^2, \quad (41)$$

$$\Delta_C = v_\sigma^2 \lambda_{16} + \frac{1}{2} v_\phi^2 \lambda_3 + v_\Sigma^2 (\lambda_{15} + \lambda_{27} + 2\lambda_{33}) + \mu_{h_2}^2. \quad (42)$$

This matrix has two non-zero eigenvalues, indicating the existence of two CP-even, CP-odd, and charged massive particles whose mass pairs are degenerate. Denoting the CP-even, CP-odd, and charged scalars by $H_{1,2}^0$, $\chi_{1,2}$, and $H_{1,2}^\pm$, their masses are:

$$m_{H_1^0}^2 = m_{\chi_1}^2 = m_{H_1^\pm}^2 = \frac{1}{8} \left(\Delta_A - \Delta_C + \sqrt{4\Delta_B^2 + (\Delta_A - \Delta_C)^2} \right), \quad (43)$$

$$m_{H_2^0}^2 = m_{\chi_2}^2 = m_{H_2^\pm}^2 = \frac{1}{8} \left(\Delta_A - \Delta_C - \sqrt{4\Delta_B^2 + (\Delta_A - \Delta_C)^2} \right). \quad (44)$$

The degeneracy in the masses of the dark scalar sector is significant, as this is a scotogenic model [47, 48]. The neutrino masses are related to the mass difference between the CP-even and CP-odd components of the inert doublets, as shown in Eq.(58) and Eq.(59). While this initially suggests massless neutrinos, the contribution of dimension-6 operators in the scalar potential breaks this degeneracy, making the mass differences proportional to Λ^{-1} and explaining the smallness of neutrino masses. For example:

$$m_{H_k^0}^2 - m_{\chi_k}^2 = \frac{v_\Sigma^2 v_\phi^2}{4\Lambda^2} (\alpha_3 + \alpha_4). \quad (45)$$

Hereafter, it is assumed that there exist values of the couplings capable of reproducing the observed neutrino mass spectrum.

IV. STANDARD MODEL FERMION MASS HIERARCHY

In this section, we demonstrate that the parameters of the fermionic sector, combined with those fitted in the scalar sector, successfully reproduce the mass hierarchy of the SM fermions.

A. Quark sector

From the interactions in Eq. (12), the mass matrices for the quark sector, M_u and M_d , are obtained in the $(u_{L1}, u_{L2}, u_{L3}, T_{L1}, T_{L2}) - (u_{R1}, u_{R2}, u_{R3}, T_{R1}, T_{R2})$ and $(d_{L1}, d_{L2}, d_{L3}, B_{L1}, B_{L2}, B_{L3}) - (d_{R1}, d_{R2}, d_{R3}, B_{R1}, B_{R2}, B_{R3})$ bases, respectively, and are expressed as:

$$M_U = \begin{pmatrix} T_u & A_u \\ B_u & C_u \end{pmatrix}, \quad M_D = \begin{pmatrix} 0_{3 \times 3} & A_d \\ B_d & C_d \end{pmatrix} \quad (46)$$

with

$$T_u = \frac{v_\phi}{\sqrt{2}} \begin{pmatrix} 0 & 0 & Y_1^1 \\ 0 & 0 & Y_2^1 \\ 0 & 0 & Y_3^1 \end{pmatrix}, \quad [A_u]_{im} = \frac{v_\phi v_\sigma}{\sqrt{2}\Lambda} Y_{im}^2, \quad [A_d]_{ij} = \frac{v_\phi v_\sigma}{\sqrt{2}\Lambda} Y_{ij}^5, \quad (47)$$

$$B_u = v_\sigma \begin{pmatrix} Y_{11}^3 & Y_{12}^3 & 0 \\ Y_{21}^3 & Y_{22}^3 & 0 \end{pmatrix}, \quad [B_d]_{ij} = v_\sigma Y_{ij}^6, \quad (48)$$

$$[C_u]_{nm} = v_\sigma Y_{nm}^4, \quad [C_d]_{ij} = v_\sigma Y_{ij}^7, \quad (49)$$

where Λ is the energy scale associated with the masses of the new exotic fermions. While the up, charm, down, bottom, and strange quarks acquire their masses through the universal seesaw mechanism, the top quark obtains its mass via the SM tree-level mechanism. The effective mass matrices for the SM quarks can be simplified as:

$$\begin{aligned} \widetilde{M}_U &= T_u - A_u C_u^{-1} B_u, \\ \widetilde{M}_D &= -A_d C_d^{-1} B_d, \end{aligned} \quad (50)$$

The quark mass hierarchy in the SM is reproduced by carefully selecting the effective parameters and the energy scale. From the previous section, we infer that the VEVs have magnitudes $\mathcal{O}(v_\phi) \sim 10^{-1}$ TeV and $\mathcal{O}(v_\sigma) \sim 10$ TeV, yielding $v_\phi v_\sigma / \Lambda \sim 1$ TeV. Parameter scans indicate that for $\Lambda \sim 10^2$ TeV, the effective parameters remain within an order of magnitude of ~ 0.1 which remains within the perturbative values.

Using the same fitting strategy as in Eq. (76), the effective parameters have been tuned to match the SM quark masses ($m_u, m_d, m_s, m_c, m_t, m_b$) [49], alongside the mixing angles ($\sin \theta_{12}^{(q)}, \sin \theta_{13}^{(q)}, \sin \theta_{23}^{(q)}$) and the Jarlskog invariant J_q [46]:

$$\begin{aligned} m_u &= (1.24 \pm 0.22) \text{ MeV}, & m_d &= (2.69 \pm 0.19) \text{ MeV}, & m_s &= (53.5 \pm 4.6) \text{ MeV}, \\ m_c &= (0.63 \pm 0.02) \text{ GeV}, & m_t &= (172.9 \pm 0.4) \text{ GeV}, & m_b &= (2.86 \pm 0.03) \text{ GeV}, \\ \sin \theta_{12}^{(q)} &= 0.2245 \pm 0.00044, & \sin \theta_{23}^{(q)} &= 0.0421 \pm 0.00076, & \sin \theta_{13}^{(q)} &= 0.00365 \pm 0.00012, \\ J_q &= (3.18 \pm 0.15) \times 10^{-5}. \end{aligned} \quad (51)$$

The main correlations between these parameters are depicted in Figure 5. Panel (a) presents the correlation matrix for the quark sector parameters, where the heatmap quantifies the strength of correlation between parameter pairs. A strong correlation is observed between $\sin \theta_{13}$ and $\sin \theta_{23}$, as well as between these angles and the Jarlskog invariant J_q . In contrast, $\sin \theta_{12}$ shows a weak correlation with J_q , aligning with experimental data. Panels (b), (c), and (d) further illustrate these relationships through scatter plots, examining specific correlations between quark mixing angles and the Jarlskog invariant. The dashed and dot-dashed lines represent experimental values from Ref. [46], enabling a visual comparison between the predictions of the model and experimental results. Within our model, values consistent with observations are achieved up to 3σ .

B. Charged lepton sector

From the fermionic sector in Eq.(12), the mass matrix for the charged lepton sector is obtained.

In the $(l_{L1}, l_{L2}, l_{L3}, E_{L1}, E_{L2}, E_{L3}) - (l_{R1}, l_{R2}, l_{R3}, E_{R1}, E_{R2}, E_{R3})$ basis, it is expressed as:

$$M_\ell = \begin{pmatrix} 0_{3 \times 3} & \frac{v_\phi}{\sqrt{2}} y_{ij}^3 \\ v_\sigma y_{ij}^1 & v_\sigma y_{ij}^2 \end{pmatrix} \quad (52)$$

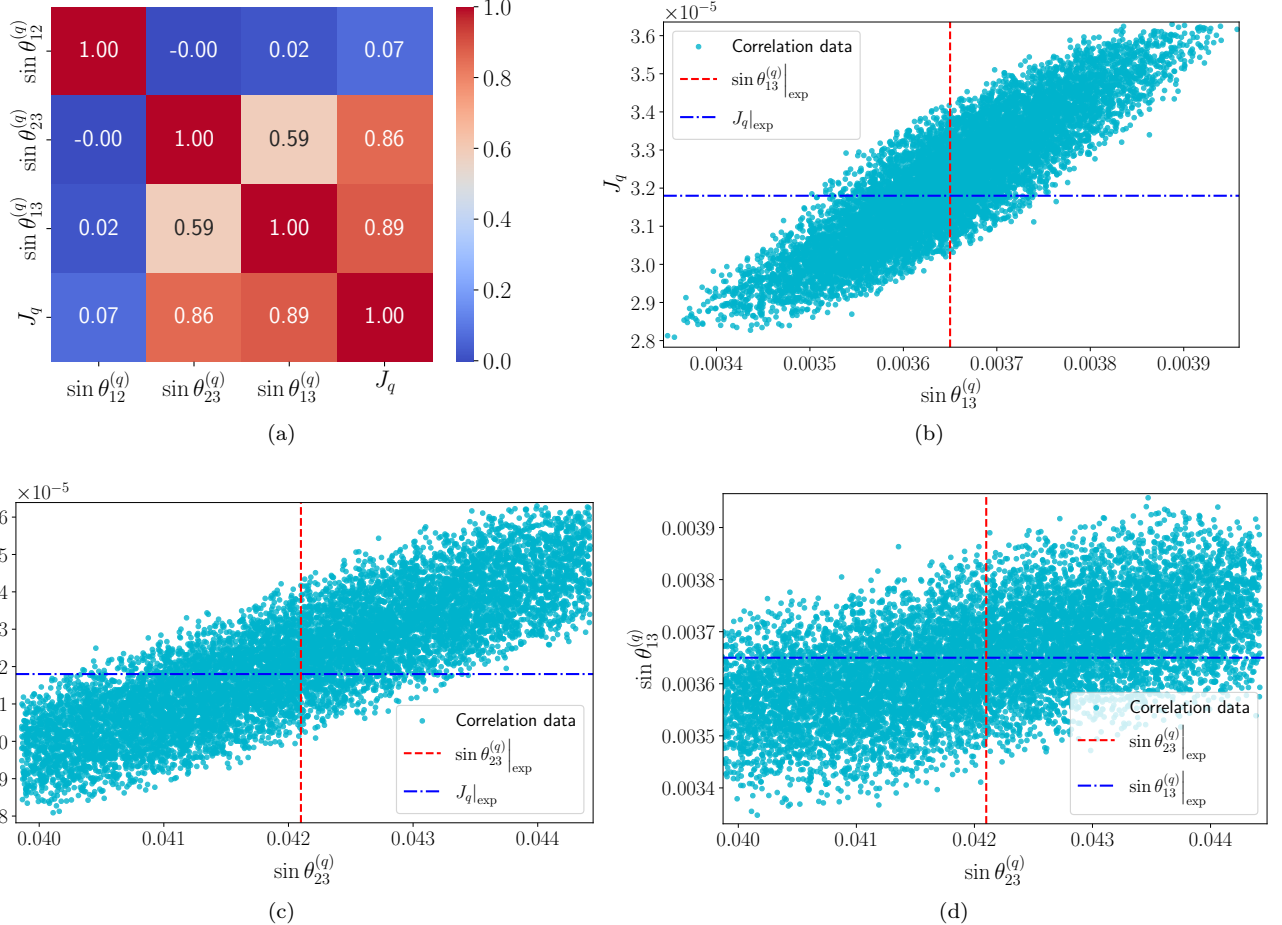


Figure 5: (a) The correlation parameter matrix of the quark sector. The color scale corresponds to the degree of correlation between two parameters. (b, c, d) Correlation plot between the mixing angles of the quarks and the Jarlskog invariant obtained with our model. The dashed and dot-dashed lines correspond to the experimental values.

To simplify the analysis, the charged lepton mass matrix can be parametrized as:

$$\widetilde{M}_\ell = A_\ell J_\ell^{-1} B_\ell^T, \quad (53)$$

where:

$$A_\ell = V_L^{(E)} M_e^{\frac{1}{2}} J_\ell^{\frac{1}{2}}, \quad B_\ell = V_R^{(E)} M_e^{\frac{1}{2}} J_\ell^{\frac{1}{2}}, \quad (54)$$

and the diagonal mass matrices are given by:

$$M_e = \text{diag}(m_e, m_\mu, m_\tau), \quad J_\ell = \text{diag}(m_{E_1}, m_{E_2}, m_{E_3}), \quad (55)$$

with $V_L^{(E)}$ and $V_R^{(E)}$ representing the rotation matrices for the left- and right-handed charged leptons, respectively. The mass hierarchy of the SM charged leptons is reproduced by exploring the parameter space, which also includes the masses of the exotic charged leptons. These masses have been set at an order of magnitude of approximately 100 TeV to ensure compatibility with the experimental values for the charged leptons (m_e, m_μ, m_τ) [50]:

$$m_e = (0.4883266 \pm 0.0000017) \text{ MeV}, \quad m_\mu = (102.87267 \pm 0.00021) \text{ MeV}, \quad m_\tau = (1747.43 \pm 0.12) \text{ MeV}. \quad (56)$$

The explicit values for the exotic charged lepton masses (in GeV) and the rotation matrices are as follows:

$$m_{E_1} = 20363.6, \quad m_{E_2} = 61432.1, \quad m_{E_3} = 14697.5,$$

$$V_L^{(E)} = \begin{pmatrix} -0.359497 & 0.769444 & 0.527937 \\ -0.528816 & -0.634131 & 0.564121 \\ 0.76884 & -0.0763817 & 0.634863 \end{pmatrix}, \quad V_R^{(E)} = \begin{pmatrix} 0.522082 & -0.752183 & 0.402058 \\ -0.417024 & 0.186082 & 0.889643 \\ 0.74399 & 0.632134 & 0.216528 \end{pmatrix}. \quad (57)$$

C. Neutrino sector

With respect to the neutrino sector, their interactions are designed to prohibit the generation of tree-level active neutrino masses, ensuring that the neutrino masses arise solely from one-loop quantum corrections. The form of the mass matrix is given by:

$$(M_\nu)_{ij} = \sum_{k=2}^3 m_N \lambda^2 y_i^{(4,5)} y_j^{(4,5)} \mathcal{F}(m_{H_k}, m_{\chi_k}, m_N), \quad (58)$$

where the loop function is defined as:

$$\mathcal{F}(m_1, m_2, m_3) = \frac{1}{16\pi^2} \left[\frac{m_1^2}{m_1^2 - m_3^2} \ln \left(\frac{m_1^2}{m_3^2} \right) - \frac{m_2^2}{m_2^2 - m_3^2} \ln \left(\frac{m_2^2}{m_3^2} \right) \right]. \quad (59)$$

The parameters of the SM neutrino sector, combined with the parameters of the PMNS matrix, are determined by exploring the values of the loop functions $\mathcal{F}(m_{H_1}, m_{\chi_1}, m_N)$ and $\mathcal{F}(m_{H_2}, m_{\chi_2}, m_N)$ and the Yukawa parameters. The reproduced observables include the experimental differences between neutrino masses (Δm_{21} , Δm_{31}), the mixing angles ($\sin^2 \theta_{12}^{(\ell)}$, $\sin^2 \theta_{13}^{(\ell)}$, $\sin^2 \theta_{23}^{(\ell)}$), and the CP-violation phase $\delta_{\text{CP}}^{(\ell)}$ [50]:

$$\Delta m_{21}^2 = 7.50_{-0.20}^{+0.22} \times 10^{-5} \text{ eV}^2, \quad \Delta m_{31}^2 = 2.55_{-0.03}^{+0.02} \times 10^{-3} \text{ eV}^2,$$

$$\sin^2 \theta_{12}^{(\ell)} = 0.318 \pm 0.016, \quad \sin^2 \theta_{23}^{(\ell)} = 0.574 \pm 0.014, \quad \sin^2 \theta_{13}^{(\ell)} = 0.02200_{-0.00062}^{+0.00069},$$

$$\delta_{\text{CP}}^{(\ell)} = (194_{-22}^{+24})^\circ.$$

Figure 6 presents the correlation analysis in the leptonic sector based on the predictions of the model. Panel (a) shows the correlation matrix of parameters, where the color scale indicates the strength of correlation between observable pairs. A strong negative correlation is observed between $\sin^2 \theta_{12}^{(\ell)}$ and the CP-violating phase $\delta_{\text{CP}}^{(\ell)}$, while $\sin^2 \theta_{13}^{(\ell)}$ and $\sin^2 \theta_{23}^{(\ell)}$ exhibit weaker correlations. Panels (b) and (c) illustrate scatter plots of these correlations, analyzing how $\delta_{\text{CP}}^{(\ell)}$ varies with $\sin^2 \theta_{12}^{(\ell)}$ and $\sin^2 \theta_{23}^{(\ell)}$, respectively. The dashed lines indicate experimental values, showing the model's ability to match observed data.

V. CONSTRAINTS FROM TRILINEAR HIGGS SEFCOUPLING H^3

The trilinear coupling of the Higgs boson, generally characterized by the parameter κ_λ , is a vital constraint for the scalar sector [51, 52]:

$$\kappa_\lambda = \frac{\lambda_{h^3}^{\text{BSM}}}{\lambda_{h^3}^{\text{SM}}}. \quad (60)$$

This parameter determines the deviation of the Higgs coupling in a BSM model relative to that in the SM. The values of the Higgs self-couplings are crucial because they characterize the shape of the Higgs field potential, which in turn establishes the structure of the SSB mechanism of the SM. This mechanism governs the dynamics of mass generation for particles acquiring mass through this process.

The most precise experimental bounds on this parameter [53] are:

$$-0.4 \leq \kappa_\lambda \leq 6.3. \quad (61)$$

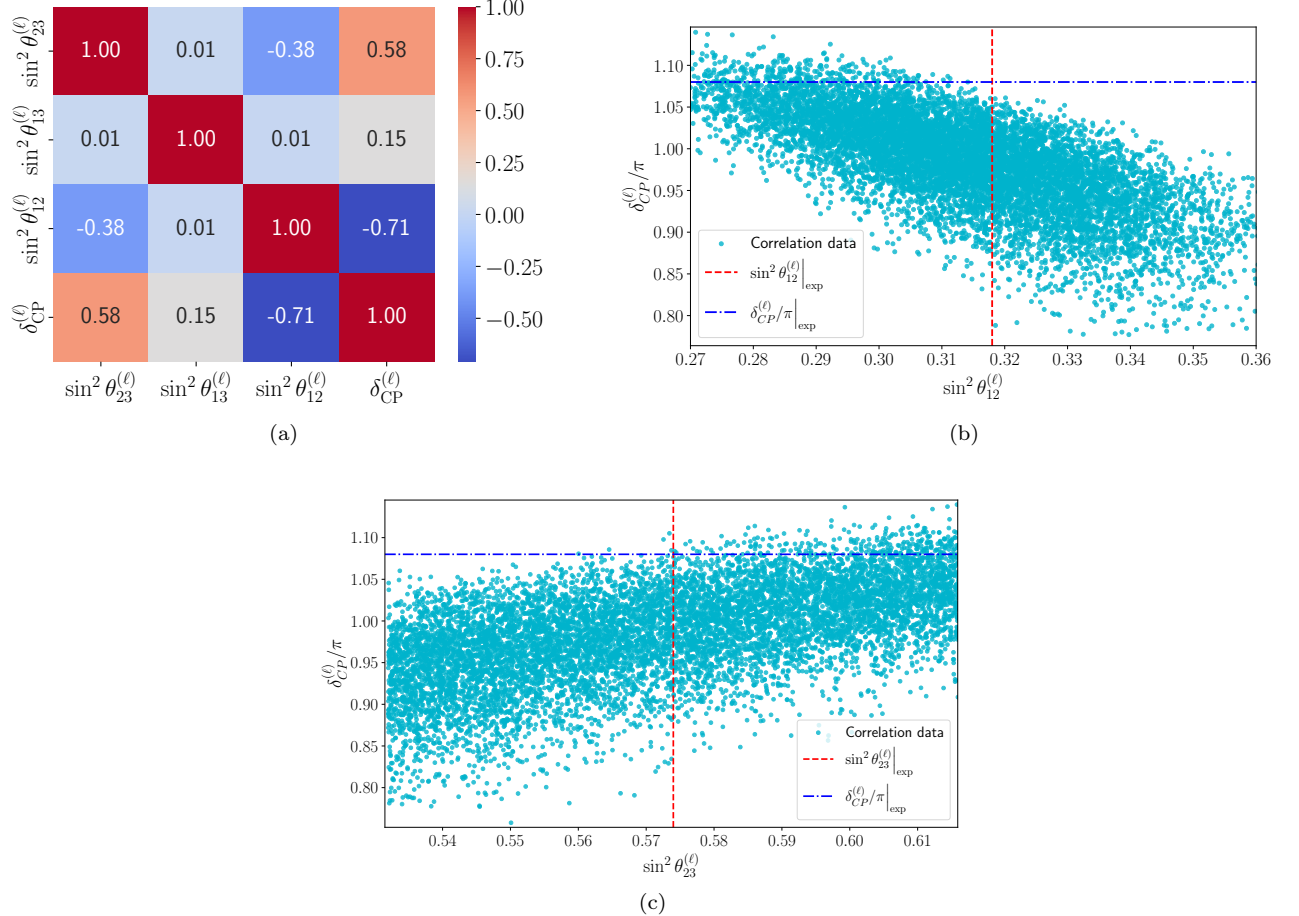


Figure 6: (a) The correlation parameter matrix of the lepton sector, where the color scale quantifies the degree of correlation between two parameters. (b, c) Scatter plots illustrating the correlations between the mixing angles in neutrino sector and $\delta_{CP}^{(\ell)}$. The dashed lines represent the experimental values, demonstrating the model's ability to replicate these observed correlations.

Incorporating these bounds, a value for the parameter κ_λ for the tree-level trilinear coupling

$$\lambda_{h^3}^{\text{BSM}} = \left. \frac{\partial^3 V_{\text{Phys}}}{\partial h^3} \right|_{\text{Fields}=0} \quad (62)$$

has been found that lies within the experimental constraints described above as can be seen in the Table III. This demonstrates that the proposed scalar sector, even with the strong dynamics associated with the new gauge symmetry, can reproduce a trilinear Higgs self-coupling consistent with current observational limits.

Beyond this, we evaluate the contribution of the scalar sector to the quantum one-loop corrections to the trilinear self-coupling. A detailed analysis of such corrections in extended Higgs sectors can be found in [54–57]. The main Feynman diagrams contributing to this correction are shown in Figure 7.

For this study, we consider the off-shell decay process $h(q) \rightarrow h(q_1)h(q_2)$, where $q_1^2 = q_2^2 = m_h^2$ and $q^2 \neq m_h^2$. The treatment of ultraviolet divergences follows the renormalization procedure outlined in [54]. The effective trilinear operator is given by:

$$\Gamma_{h^3}^R(q^2) = \lambda_{h^3}^{\text{BSM}} + \Gamma_{h^3}^{\text{1-loop}}(q^2) + \delta\Gamma_{h^3}, \quad (63)$$

where $\Gamma_{h^3}^R$ is the one-loop renormalized operator, $\Gamma_{h^3}^{\text{1-loop}}$ represents the contribution from the Feynman diagrams in Figure 7, and $\delta\Gamma_{h^3}$ accounts for the counterterm contributions. The explicit form of the one-loop terms can be found in Appendix C.

The magnitude of the one-loop corrections is illustrated through the ratio:

$$\Delta\Gamma_{h^3}^{1\text{-loop}}(q^2) = \frac{\Gamma_{h^3}^R(q^2)}{\lambda_{h^3}^{\text{SM}}}. \quad (64)$$

Numerical analysis reveals that, for our benchmark point, the renormalized effective coupling takes the value:

$$\Delta\Gamma_{h^3}^{1\text{-loop}}(q^2 = M_Z^2) = 0.34437. \quad (65)$$

This result indicates that radiative corrections shift the effective trilinear self-coupling away from the standard tree-level prediction; however, the deviation remains within the experimentally allowed range and does not lead to significant discrepancies. Figure 8(a) illustrates that, by varying the masses of the exotic scalars between 500 GeV and 10 TeV while keeping the energy scale at the Z boson mass, there are values for the one-loop corrections that remain consistent with experimental constraints.

Alternatively, we can analyze the deviation in the squared amplitude respect to the SM contribution by defining

$$\Delta|\Gamma_{h^3}(q^2)| = \sqrt{\frac{|\Gamma_{h^3}^R(q^2) + \lambda_{h^3}^{\text{BSM}}\Gamma_{h^3}^{SM}|^2}{|\lambda_{h^3}^{\text{SM}}(1 + \Gamma_{h^3}^{SM})|^2}}, \quad (66)$$

where $\Gamma_{h^3}^{SM}$ is the leading contribution of the SM to the effective coupling which will be considered only the correction due to the top quark [58, 59]

$$\Gamma_{h^3}^{SM} = -\frac{N_c}{3\pi^2} \frac{m_t^4}{v_\phi^2 m_h^2} \left\{ 1 + \mathcal{O}(\text{External momenta}) \right\}. \quad (67)$$

In this case, the interference between both contributions leads to different outcomes. As shown in Figure 8(b), varying the masses of the exotic scalars within the range of 500 GeV to 10 TeV can result in moderate percentage deviations of the radiative corrections from the exotic scalar sector relative to the dominant SM corrections. Notably, for our benchmark point (marked by the green star), the deviation is given by $\Delta|\Gamma_{h^3}(q^2)| = 0.394299$ which still agree with the experimental bounds.

VI. HIGGS DIPHOTON RATE

The insertion of a strong sector in models with an extended number of higgs doublets can be a good approach in order to constrain the parametric space of that models, for example, this has been explored in a 2HDM models. In order to study the implications of the extra inert doublets in the decay of the 126 GeV Higgs into a photon pair³, one introduces the Higgs diphoton signal strength $R_{\gamma\gamma}$, which is defined as:

$$R_{\gamma\gamma} = \frac{\sigma(pp \rightarrow h)_{\text{BSM}}\Gamma(h \rightarrow \gamma\gamma)_{\text{BSM}}}{\sigma(pp \rightarrow h)_{\text{SM}}\Gamma(h \rightarrow \gamma\gamma)_{\text{SM}}}, \quad (68)$$

where the expression is normalized by the $\gamma\gamma$ signal in the SM. The dominant channel for Higgs boson production is gluon fusion, mediated by a top quark loop, therefore we can use the approximation $\sigma(pp \rightarrow h)_{\text{BSM}} \simeq \mathcal{A}_{htt}^2 \sigma(pp \rightarrow h)_{\text{SM}}$, and the ratio $R_{\gamma\gamma}$ will involve only the Higgs decays.

In the SM, the Higgs boson decay width into two photons is dominated by the interference between the W -boson and the top quark, meanwhile, in our model the presence of non-SM fields introduce loop corrections to the total amplitude of the decay. In Figure 9 the new one-loop Feynman diagrams can be seen.

³ The $\gamma\gamma$ channel is not the unique contribution to the total width of the Higgs boson decay, in a more complete study it is important to consider fermionic $c\bar{c}, b\bar{b}, \tau^+\tau^-$ and vector $Z\gamma, W^+W^-, GG, \gamma\gamma$ decay channels, as well as additional invisible Higgs decay channels to scalar H_k and pseudoscalar χ_k particles. For the regions where masses of scalar and pseudo-scalar $M_{H_k}(M_{\chi_k}) > m_h$, the invisible decay channels are kinematically closed.

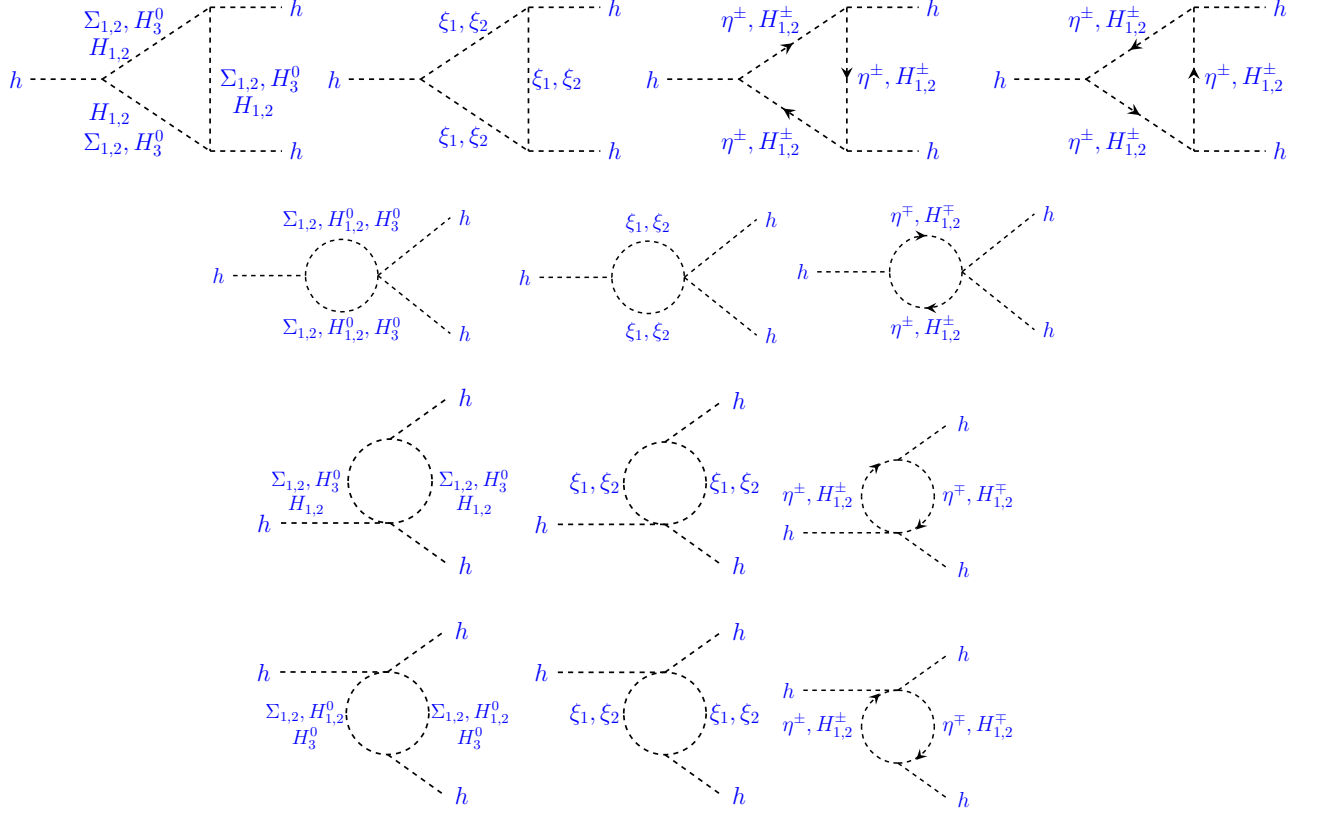


Figure 7: Extra one-loop Feynman diagrams in the unitary gauge contributing to the Higgs trilinear selfcoupling.

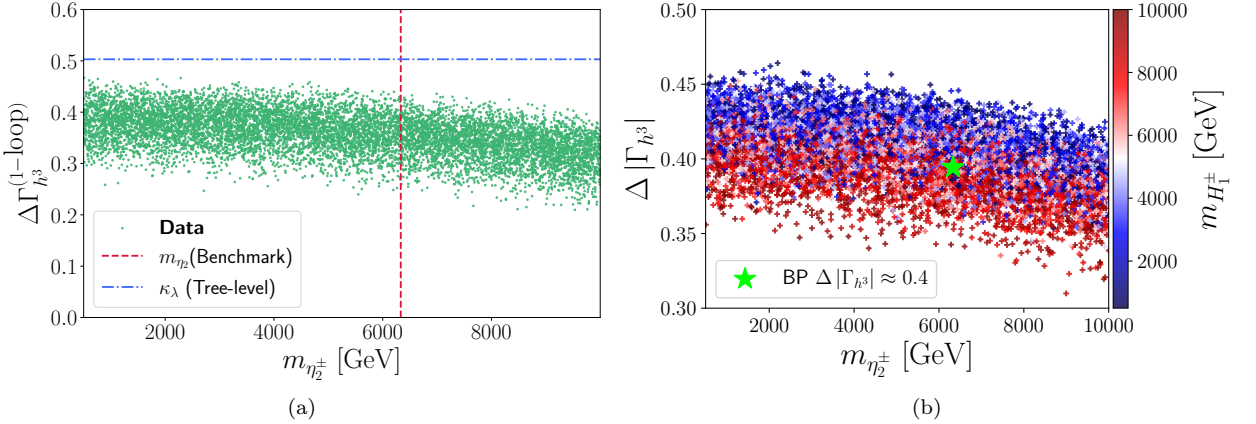


Figure 8: One-loop radiative correction to the Higgs trilinear self-coupling. Panel (a) shows the variation of $\Delta\Gamma_{h^3}^{1\text{-loop}}$ for different masses of the exotic scalars, evaluated at the energy scale corresponding to the Z boson mass. Panel (b) presents the deviation of the radiative corrections from the new scalar sector of the model relative to the leading SM radiative corrections as a function of the exotic particle masses at the energy scale $q = M_Z$. The green star represents the deviation at our benchmark point.

The decay amplitude for the $h \rightarrow \gamma\gamma$ process takes the form [60–63]:

$$\Gamma(h \rightarrow \gamma\gamma) = \frac{\alpha_{\text{em}}^2 m_h^3}{256\pi^3 v_\phi^2} \left| N_C \sum_f Q_f^2 \mathcal{A}_{hff} F_{\frac{1}{2}}(\varrho_f) + \mathcal{A}_{hWW} F_1(\varrho_W) + \mathcal{A}_{h\eta^\pm\eta^\mp} F_0(\varrho_{\eta^\pm}) + \mathcal{A}_{h\rho^\pm\rho^\mp} F_1(\varrho_{\rho^\pm}) \right|^2, \quad (69)$$

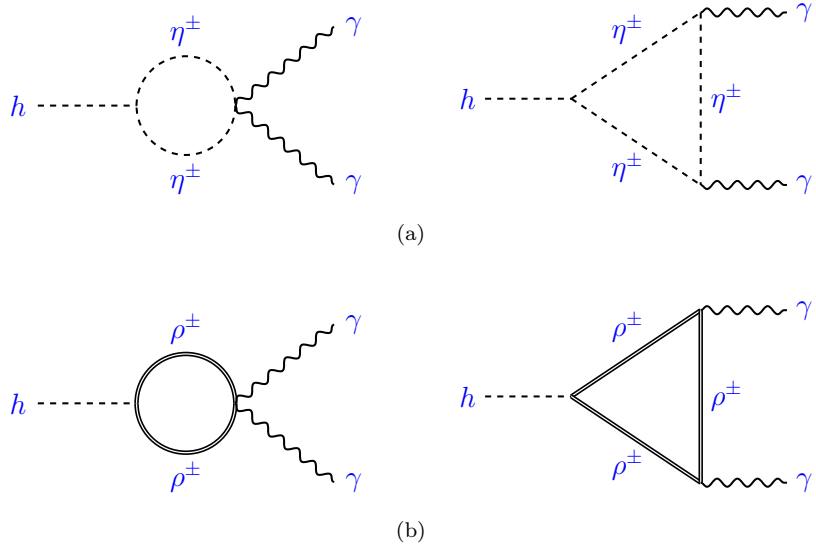


Figure 9: Extra one-loop Feynman diagrams in the unitary gauge contributing to the Higgs diphoton decay. In (a) the new charged scalars contribution and in (b) the vector resonances contributions

where α_{em} is the fine-structure constant, N_C is the color factor ($N_C = 3$ for quarks and $N_C = 1$ for leptons) and Q_f is the electric charge of the fermion in the loop. The most significant contribution to the fermionic loop comes from the top quark, and it will be the only one considered. Here, ϱ represents the mass ratio $\varrho_i = 4M_i^2/m_h^2$ with $M_i = m_f, M_W, M_{\rho^\pm}, M_{\eta^\pm}$ and $k = 1, 2$. Furthermore \mathcal{A}_{hff} and \mathcal{A}_{hWW} are the deviation factors (normalized by the mass) from the SM Higgs-quark coupling and the SM Higgs-W gauge boson coupling respectively, in the SM for the quark top the factor $\mathcal{A}_{htt} \simeq 1$ whereas the factor \mathcal{A}_{hWW} can be written in the following form

$$\mathcal{A}_{hWW} = \frac{1}{2} \frac{v_\phi}{M_{W^\pm}^2} \left. \frac{\partial^3 \mathcal{L}_{\text{gauge,Phys}}}{\partial h \partial W^\pm \partial W^\mp} \right|_{\text{Fields}=0}, \quad (70)$$

and the SM like Higgs -charged Higgs boson and -vector resonance trilineal couplings are respectively

$$\begin{aligned} \mathcal{A}_{h\eta^\pm\eta^\mp} &= \frac{1}{2} \frac{v_\phi}{M_{\eta^\pm}^2} \left. \frac{\partial^3 V_{\text{Phys}}}{\partial h \partial \eta^\pm \partial \eta^\mp} \right|_{\text{Fields}=0}, \\ \mathcal{A}_{h\rho^\pm\rho^\mp} &= \frac{1}{2} \frac{v_\phi}{M_{\rho^\pm}^2} \left. \frac{\partial^3 \mathcal{L}_{\text{gauge,Phys}}}{\partial h \partial \rho^\pm \partial \rho^\mp} \right|_{\text{Fields}=0}. \end{aligned} \quad (71)$$

The form factors for the contributions of particles with spin-0, 1/2 and 1 are:

$$F_0(\varrho) = -\varrho(1 - \varrho f(\varrho)), \quad (72)$$

$$F_{\frac{1}{2}}(\varrho) = 2\varrho(1 + (1 - \varrho)f(\varrho)), \quad (73)$$

$$F_1(\varrho) = -(2 + 3\varrho + 3\varrho(2 - \varrho)f(\varrho)), \quad (74)$$

with

$$f(\varrho) = \begin{cases} \arcsin^2 \sqrt{\varrho^{-1}}, & \text{for } \varrho \geq 1, \\ -\frac{1}{4} \left[\ln \left(\frac{1+\sqrt{1-\varrho}}{1-\sqrt{1-\varrho}} \right) - i\pi \right]^2, & \text{for } \varrho < 1. \end{cases} \quad (75)$$

The decay rate in conjunction with the standard model scalar masses and couplings will be used to restrict the parametric space of the model. The couplings have been scanned over a range of numerical values compatible with the perturbative renormalization group, excepting for the g_2 coupling, on which the underlying strong sector is based. The parameters include the quartic couplings of the scalar potential, the VEVs of the Σ and σ fields, the coupling constants of the gauge group $SU(2)_2 \times SU(2)_1 \times U(1)_Y$, the decay parameter of the nonlinear Goldstone bosons f_Σ , the β parameter, and the mixing angles.

Observable	Model Value	Experimental Value
m_h	125.245 GeV	(125.25 ± 0.17) GeV [46]
M_W	80.377 GeV	(80.377 ± 0.012) GeV [46]
M_Z	91.1876 GeV	(91.1876 ± 0.0021) GeV [46]
A_{hWW}	1.00464	1.035 ± 0.031 [64]
$R_{h\gamma\gamma}$	0.994229	$1.04^{+0.10}_{-0.09}$ [65]
κ_λ	0.503052	$[-0.4, 6.3]$ [53]

Table III: Comparison between predicted and experimental values of key observables in the model.

Among the restrictions imposed on the parameter space are masses of the order of 1 TeV for new particles, in order to elude the LHC constraints on the detection of new particles, including strong vector resonances, and to place the exotic VEVs at a high scale of about 10 TeV. Phenomenological constraints on the scan dictate that the parameter space reproduces the Higgs and W, Z boson masses, the trilinear coupling between the Higgs and W boson in Eq.(70), the Higgs trilinear self-coupling in Eq.(61) and the Higgs into two photons decay rate within a deviation of 3σ .

The adjustment strategy is based on the minimization of a χ^2 function:

$$\chi^2 = \sum_{o=1}^n \frac{(\mathcal{N}_{o,\text{model}} - \mathcal{N}_{o,\text{exp}})^2}{(\Delta \mathcal{N}_o)^2}, \quad (76)$$

where $\mathcal{N}_{o,\text{model}}$ and $\mathcal{N}_{o,\text{exp}}$ refer to the numerical values of a physical observable predicted by the model with given parameter values and the experimental measurement of that observable and $\Delta \mathcal{N}_o$ is the reported error for the observable up to 3σ of deviation⁴.

The best fit was found by preliminarily adjusting the boson masses, thereby finding a set of values over which the χ^2 function is minimized through a random value scan equipped with a logic gate that selects smaller and smaller values of χ^2 , while discarding values that violate the stability conditions of the scalar potential in (30).

The best-fit values for the main input parameters are:

$$f_\Sigma = 0.0553262, \quad v_\Sigma = 17317.3 \text{ GeV}, \quad v_\sigma = 5044.37 \text{ GeV}, \quad \beta = 2.89831 \times 10^{-4} \text{ GeV}^{-1}, \quad (77)$$

which yield the numerical values of the observables summarized in Table III.

The Figure 10 shows the dependence of the decay rate $R_{\gamma\gamma}$ with respect to the strong vector resonance mass ρ^\pm for different values of the dimensionless parameter β . The blue solid line represents the case of the fit performed for β in our model, in addition, the magenta dashed line corresponds to $\beta = 0$ and green dash-dotted line corresponds to $\beta = 1$. In the region $M_{\rho^\pm} > 500$ GeV, the value of the ratio $R_{\gamma\gamma}$ stabilizes, tending to the best fit represented by the triangular points in the figure. The experimental predictions of CMS and ATLAS are also included. This shows that although certain parameters, such as the trilinear coupling between the Higgs and the W boson, are sensitive to the parameter β , the observables still show stability to changes in this parameter. This allows the theory to behave well both in the absence of this parameter and for values in the perturbative regime.

Finally, the significance of our result for $R_{\gamma\gamma}$ is contained in the present observations, suggesting that the theoretical framework revealed by our work could explain different deviations in the diphoton signal in future experiments. Theoretically, these deviations result from the incorporation of additional Feynman diagrams due to the new particles proposed by the model, modifying not only the decay signal but also the possible experimental signals. Any significant deviation could be a direct indication of the presence of new physics. In this sense, our results highlight the importance of considering these additional loop effects in the experimental analysis in order to discriminate between SM and BSM model predictions.

VII. THE CHARGED LEPTON FLAVOR VIOLATING PROCESSES

The SM indicates that leptonic flavor is an invariant quantity, such that in any interaction process involving SM leptons, the total flavor is globally preserved. However, this does not preclude the possibility of flavor violations in

⁴ The symbol σ is used in the χ^2 function. It is a symbol different from the singlet scalar field in this model.

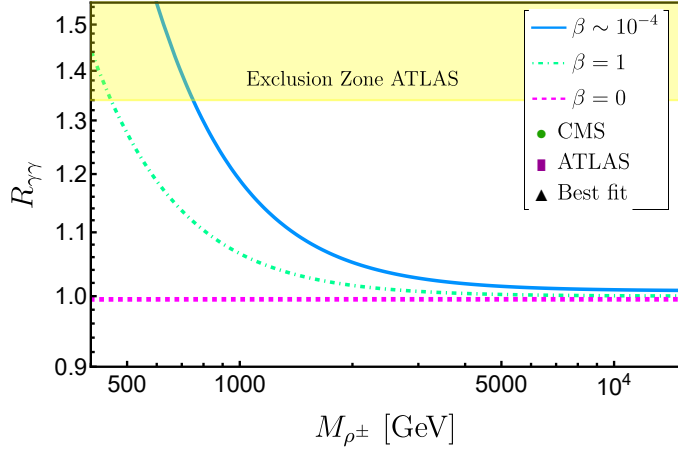


Figure 10: The ratio $R_{\gamma\gamma}$ as a function of M_{ρ^\pm} for several values of β parameter. The circle and box correspond to the experimental predictions of the CMS $1.02^{+0.11}_{-0.09}$ [66] and ATLAS $1.04^{+0.10}_{-0.09}$ [65] collaborations, respectively, the triangle points correspond to best fit for our model. The shaded region corresponds to an exclusion zone superior to 3σ for the result of the CMS collaborations.

other particles, such as quarks, within the SM. The reason for this distinction between leptons and quarks remains a significant challenge in particle physics. On the other hand, neutrino oscillations demonstrate that lepton flavor is not a true symmetry of nature, suggesting the existence of charged lepton flavor-violating (CLFV) processes.

To date, CLFV processes have not been directly observed. However, at higher energy scales, it is anticipated that such flavor violations could be detected in charged lepton interactions, similar to those observed in neutrinos. Within the SM, CLFV processes are suppressed by the Glashow–Iliopoulos–Maiani (GIM) mechanism to $\mathcal{O}(10^{-50})$ [67], making them unobservable in practice. BSM frameworks provide promising scenarios where measurable CLFV processes could occur. The most stringent limits for CLFV are derived from measurements of decays involving a charged lepton into another charged lepton and a photon; specifically, the upper limit corresponds to the muon decay $\mu \rightarrow e\gamma$.

Due to the preserved \mathbb{Z}'_2 symmetry, the extra scalars h_k do not acquire VEVs, and therefore the neutrino masses do not arise at tree level. Consequently, the non-renormalizable operators, $\frac{1}{\Lambda} \overline{L}_L^i \tilde{h}_k \Sigma N_R$, induce lepton flavor-violating decays, occurring at one-loop as depicted in Figure 11(a). The branching ratio (Br) for $\ell_i \rightarrow \ell_j \gamma$ is given by [36, 68–70]:

$$\text{Br}(\ell_i \rightarrow \ell_j \gamma) = \frac{3(4\pi)^3 \alpha_{\text{em}}}{4G_F^2} \left| A_D^{(i,j)} \right|^2 \text{Br}(\ell_i \rightarrow \ell_j \nu_i \bar{\nu}_j), \quad (78)$$

where $i \neq j$, and G_F is the Fermi constant. The amplitude coming from the dipole-photon penguin diagram Figure 11 (a), usually known as the dipole form factor, is related to the transition magnetic moment between the lepton ℓ_j and the lepton ℓ_i . In this case, i, j are flavor indices, and it is defined as:

$$A_D^{(i,j)} = \frac{x_i^{(4,5)} x_j^{(4,5)}}{2(4\pi)^2 m_{\eta^\pm}^2} F_2(\xi_{\eta^\pm}^2), \quad (79)$$

where $x_i^{(4,5)} = \sum_{k=1}^3 y_k^{(4,5)} (V_{\ell L}^\dagger)_{ik}$, the mass ratio $\xi_{\eta^\pm} = m_N/m_{\eta^\pm}$, and $V_{\ell L}$ is the mixing matrix of the left-handed charged leptons. The loop function $F_2(x)$ is given by:

$$F_2(x) = \frac{1 - 6x + 3x^2 + 2x^3 - 6x^2 \log x}{6(1-x)^4}. \quad (80)$$

Figure 12 illustrates the relationship between the branching ratio for the CLFV process $\mu \rightarrow e\gamma$ and the charged scalar mass m_{η^\pm} , with a color gradient representing the range of heavy neutrino masses m_N . The scatter points depict the branching ratio as a function of m_{η^\pm} , showing that as the charged scalar mass increases, the branching ratio significantly decreases. The exclusion zone from the MEG-2016 experiment [71], corresponding to an upper limit of 4.2×10^{-13} for $\text{Br}(\mu \rightarrow e\gamma)$, is represented by the shaded region. Points within this region are excluded by current experimental data, while points below it are consistent with experimental constraints. The gradient colors, ranging from purple to yellow, indicate different values of m_N , with heavier neutrino masses favoring higher branching ratios.

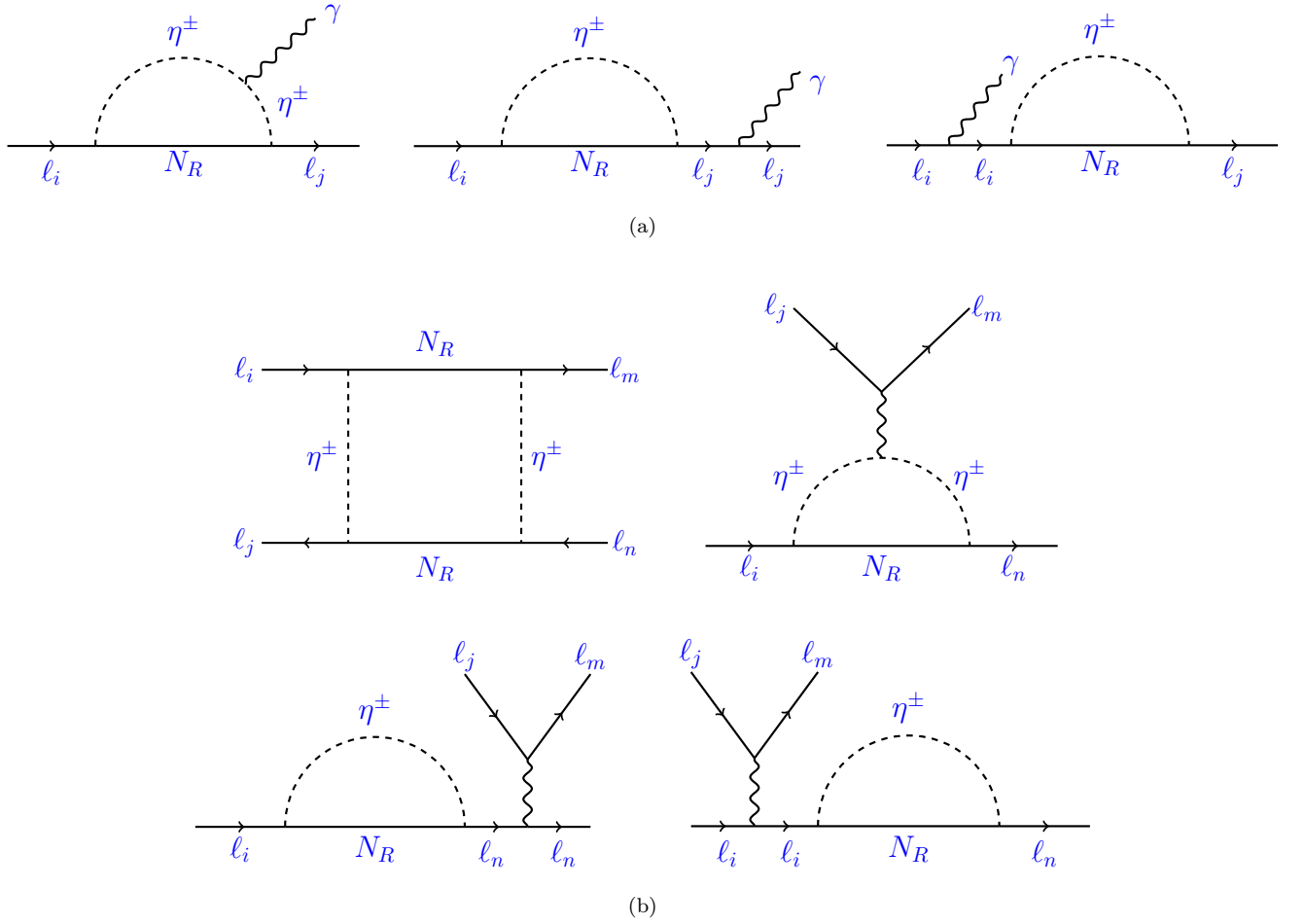


Figure 11: The one-loop Feynman diagrams leading to CLFV processes. In (a) the dipole-photon penguin diagrams contribution to $\ell_i \rightarrow \ell_j \gamma$ and in (b) the non-dipole photon penguin diagrams and box diagram contribution to $\ell_i \rightarrow \ell_j \ell_m \ell_n$

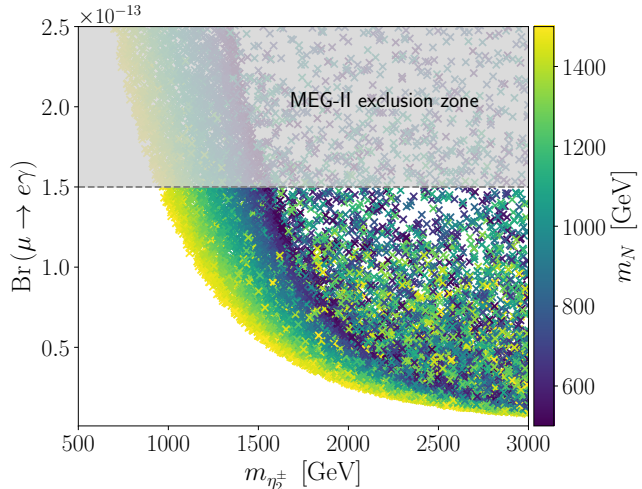


Figure 12: Branching ratio $\text{Br}(\mu \rightarrow e\gamma)$ as a function of the mass of charged scalar masses $m_{\eta_2^\pm}$ and the color represents the scan in the plane m_N - $m_{\eta_2^\pm}$. The shadowed region is excluded by MEG II [72].

Another important leptonic flavor violation observable is the branching ratio for 3-body decays $\ell_i \rightarrow 3\ell_j$, which is given by:

$$\text{Br}(\ell_i \rightarrow \ell_j \bar{\ell}_j \ell_j) = \frac{3(4\pi)^2 \alpha_{\text{em}}^2}{8G_F^2} \left[\left| A_{ND}^{(i,j)} \right|^2 + \left| A_D^{(i,j)} \right|^2 \left(\frac{16}{3} \log \left(\frac{m_i}{m_j} \right) - \frac{22}{3} \right) + \frac{1}{6} \left| B^{(i,j)} \right|^2 \right. \\ \left. + \left(-2A_{ND}^{(i,j)} A_D^{(i,j)*} + \frac{1}{3} A_{ND}^{(i,j)} B^{(i,j)*} - \frac{2}{3} A_D^{(i,j)} B^{(i,j)*} + H.c. \right) \right] \text{Br}(\ell_i \rightarrow \ell_j \nu_i \bar{\nu}_j), \quad (81)$$

where $A_{ND}^{(i,j)}$ is the non-dipole photon penguin diagram contribution, and $B^{(i,j)}$ is the contribution arising from the box diagram of Figure 11 (b). They can be expressed as:

$$A_{ND}^{(i,j)} = \sum_{k=1}^2 \frac{x_{i,k} x_{j,k}^*}{6(4\pi)^2} \frac{1}{m_{\eta_k^\pm}^2} G_2 \left(\xi_{\eta_k^\pm}^2 \right), \quad (82)$$

$$e^2 B^{(i,j)} = \frac{1}{(4\pi)^2 m_{\eta_k^\pm}^2} \sum_{k=1}^2 \left[\frac{1}{2} |x_{j,k}|^2 x_{j,k}^* x_{i,k} D_1 \left(\xi_{\eta_k^\pm}^2 \right) + \xi_{\eta_k^\pm}^2 |x_{j,k}|^2 x_{j,k}^* x_{i,k} D_2 \left(\xi_{\eta_k^\pm}^2 \right) \right]. \quad (83)$$

The different loop functions are given by [63]:

$$G_2(\varrho) = \frac{2 - 9\varrho + 18\varrho^2 - 11\varrho^3 + 6\varrho^4 \log \varrho}{6(1 - \varrho)^4}, \\ D_1(\varrho) = \frac{-\varrho^2 + 2\varrho \log(\varrho) + 1}{(\varrho - 1)^3}, \\ D_2(\varrho) = \frac{-2\varrho + (\varrho + 1) \log(\varrho) + 2}{(\varrho - 1)^3}. \quad (84)$$

The μ - e conversion in nuclei is another significant CLFV process, where a muon is converted into an electron in the presence of a nucleus. The conversion rate, denoted as $\text{CR}(\mu - e)$, quantifies the probability of this transition occurring within the atomic environment. This process is particularly sensitive to new physics contributions arising in BSM extensions like the one considered in this work, and provides complementary constraints to those obtained from other CLFV processes, such as $\mu \rightarrow e\gamma$. The branching ratio for $\mu^- - e^-$ conversion is defined as follows [73]:

$$\text{CR}(\mu - e) = \frac{\Gamma(\mu^- + \text{Nucleus}(A, Z) \rightarrow e^- + \text{Nucleus}(A, Z))}{\Gamma(\mu^- + \text{Nucleus}(A, Z) \rightarrow \nu_\mu + \text{Nucleus}(A, Z - 1))}. \quad (85)$$

For the radiative neutrino mass model considered in this work, the conversion rate, normalized to the charged lepton capture rate, takes the form [69]:

$$\text{CR}(\ell_i N \rightarrow \ell_j N) = \frac{p_j E_j m_i^3 G_F^2 \alpha_{\text{em}}^3 Z_{\text{eff}}^4 F_p^2}{8\pi^2 Z \Gamma_{\text{capt}}} \left[\left| (Z + N) \left(g_{LV}^{(0)} + g_{LS}^{(0)} \right) + (Z - N) \left(g_{LV}^{(1)} + g_{LS}^{(1)} \right) \right|^2 \right. \\ \left. + \left| (Z + N) \left(g_{RV}^{(0)} + g_{RS}^{(0)} \right) + (Z - N) \left(g_{RV}^{(1)} + g_{RS}^{(1)} \right) \right|^2 \right], \quad (86)$$

where Z and N are the number of protons and neutrons in the nucleus, Z_{eff} is the effective atomic charge [74], F_p denotes the nuclear matrix element, and Γ_{capt} represents the total muon capture rate. Numerical values extracted from [75] are presented in Table IV. The coupling constants $g_{L/R;S/V}^{(0,1)}$ are given by:

$$g_{L/R;S/V}^{(0,1)} = \frac{1}{2} \sum_{q=u,d,s} \left(g_{L/R;S/V(q)} G_{S,V}^{(q,p)} \pm g_{L/R;S/V(q)} G_{S,V}^{(q,n)} \right), \quad (87)$$

where the numerical values of the $G_{S,V}$ coefficients can be found in [76].

In Figure 13, the correlation between the CLFV processes $\mu \rightarrow e$ conversion in aluminum nuclei and $\mu \rightarrow e\gamma$ is illustrated. The points are color-coded based on the branching ratio of the $\mu \rightarrow eee$ process, as indicated by the color bar. The current experimental upper limits for these processes are shown as solid blue lines: $\text{Br}(\mu \rightarrow e\gamma) < 1.5 \times 10^{-13}$ [72] and $\text{Cr}(\mu \text{Ti} \rightarrow e \text{Ti}) < 6.1 \times 10^{-13}$ [77]. The projected future sensitivities are marked by dashed blue lines: $\text{Br}(\mu \rightarrow e\gamma) < 4 \times 10^{-14}$ [78] and $\text{Cr}(\mu \text{Al} \rightarrow e \text{Al}) \lesssim 10^{-17}$ [79].

Z^A Nucleus	Z_{eff}	F_p	Γ_{capt} (GeV)
$^{48}_{22}\text{Ti}$	17.6	0.54	1.70422×10^{-18}
$^{197}_{51}\text{Au}$	33.5	0.16	8.59868×10^{-18}
$^{27}_{13}\text{Al}$	11.5	0.64	4.64079×10^{-19}

Table IV: Values of Z_{eff} , F_p , and Γ_{capt} for Titanium, Gold, and Aluminum nuclei [75].

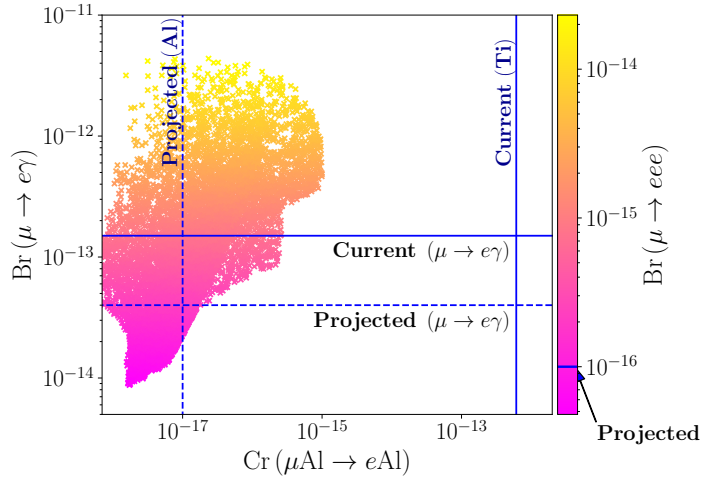


Figure 13: Correlation between the LFV processes $\mu \rightarrow e$ conversion in aluminum nuclei and $\mu \rightarrow e\gamma$. The points are color-coded according to the branching ratio of the $\mu \rightarrow eee$ process, as shown in the color bars. The current upper bounds are indicated by the solid blue lines, while the future sensitivities are marked by the dashed blue lines. The bars indicate the projected bounds for $\mu \rightarrow eee$.

Additionally, the bars indicate the projected bounds for the $\mu \rightarrow e$ conversion in aluminum (Al) [80] and titanium (Ti) [81] nuclei, allowing for a visual comparison between current constraints and those anticipated from future experimental upgrades. This correlation is crucial for evaluating the sensitivity of upcoming experiments in probing LFV processes and exploring a broader range of model parameters.

VIII. LEPTOGENESIS

One of the central challenges in modern physics is understanding the baryon asymmetry of the Universe, which underpins the observed dominance of matter over antimatter. A dynamic explanation is often favored, as any preexisting asymmetry would likely have been erased by a potential cosmic inflationary period preceding the Big Bang. The current baryon asymmetry is quantified by the dimensionless parameter [1]:

$$Y_{\Delta B} = \frac{n_B - n_{\bar{B}}}{s} = (0.87 \pm 0.01) \times 10^{-10}, \quad (88)$$

where n_B and $n_{\bar{B}}$ represent the number densities of baryons and antibaryons, respectively, and s denotes the entropy density.

For a physical model to generate a baryon asymmetry dynamically, it must satisfy the three Sakharov conditions [82]: (i) baryon number violation to enable a non-zero $Y_{\Delta B}$; (ii) violation of C and CP symmetries, allowing different dynamics for baryons and antibaryons; and (iii) a departure from thermal equilibrium to permit an asymmetry in number densities. While the SM accommodates these conditions in principle, the suppression of CP -violating effects and the insufficient strength of the baryon-number-violating processes render its contribution negligible, necessitating physics beyond the SM.

Leptogenesis offers an elegant mechanism by converting an initial lepton asymmetry into a baryon asymmetry through electroweak sphaleron processes. These processes violate the anomalous $B + L$ symmetry, while conserving $B - L$, enabling the transfer of a lepton asymmetry into the baryon sector. The topological nature of this anomaly plays

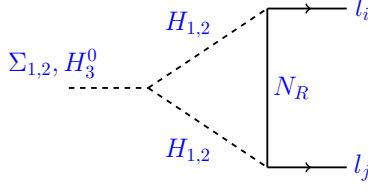


Figure 14: One-loop contribution to lepton number violation processes.

a critical role, as sphaleron-induced transitions between distinct vacuum configurations of the gauge fields are non-perturbative phenomena that efficiently convert lepton number into baryon number in the early Universe.

A. Lepton asymmetry parameter

Our model predicts radiatively induced processes that violate lepton flavor, as illustrated in Figure 14. These processes emerge naturally from the extended scalar sector and the introduction of exotic doublets, which mediate flavor transitions through loop-level corrections. The associated asymmetry parameters, which quantify the generated lepton number violation, are defined as [83–85]:

$$\begin{aligned} \epsilon_{S_\alpha} &= 2 \frac{\Gamma(S_\alpha \rightarrow l_i l_j) - \Gamma(S_\alpha \rightarrow \bar{l}_i \bar{l}_j)}{\Gamma(S_\alpha \rightarrow l_i l_j) + \Gamma(S_\alpha \rightarrow \bar{l}_i \bar{l}_j)} \\ &= \frac{m_N}{2\pi} \frac{v_\Sigma}{\sqrt{2}} \frac{\sum \text{Im} [y_i^4 y_i^4 C_{S_\alpha h_1 h_1} + y_i^4 y_i^5 C_{S_\alpha h_1 h_2} + y_i^5 y_i^5 C_{S_\alpha h_2 h_2}]}{C_{S_\alpha h_1 h_1}^2 + C_{S_\alpha h_1 h_2}^2 + C_{S_\alpha h_2 h_2}^2} \ln \left(1 + \frac{m_{S_\alpha}^2}{m_N^2} \right), \end{aligned} \quad (89)$$

where $S_\alpha = \Sigma_1, \Sigma_2, H_3^0$. On the other hand, the total decay width of the S_α particle is given by

$$\Gamma_{S_\alpha T} = \Gamma(S_\alpha \rightarrow l_i l_j) + \Gamma(S_\alpha \rightarrow \bar{l}_i \bar{l}_j) = \frac{1}{8\pi} \left[\frac{C_{S_\alpha h_1 h_1}^2 + C_{S_\alpha h_1 h_2}^2 + C_{S_\alpha h_2 h_2}^2}{m_{S_\alpha}} \right]. \quad (90)$$

In Figure 15, we present the dependence of the asymmetry parameters on the masses of the scalars and heavy neutrinos. The results indicate a partial dominance of the CP asymmetry arising from the decay of the Σ_2 scalar. This is due to its slightly weaker coupling with the inert scalars, which contributes to a higher asymmetry parameter. Specifically, the asymmetry parameter associated with this decay is approximately one order of magnitude larger than those corresponding to other scalar decay processes.

B. Baryon Asymmetry Parameter

In order to test the capabilities of this model in leptogenesis processes we will estimate the baryonic asymmetry parameter, without resorting to explicitly solve the Boltzman equation, which is beyond the scope of this work.

We will start by calculating the washout parameters associated to each of the scalars as

$$K_\alpha = \left. \frac{\Gamma_{S_\alpha T}}{2H(T)} \right|_{T=m_{S_\alpha}}, \quad (91)$$

where $H(T)$ is the Hubble constant as function of the temperature

$$H(T) = \sqrt{\frac{8\pi^3 g_*}{90}} \frac{T^2}{M_{\text{Pl}}}, \quad (92)$$

$g_* = 114.75$ is the number of relativistic degrees of freedom and $M_{\text{Pl}} = 1.22 \times 10^{19}$ GeV is the Planck mass.

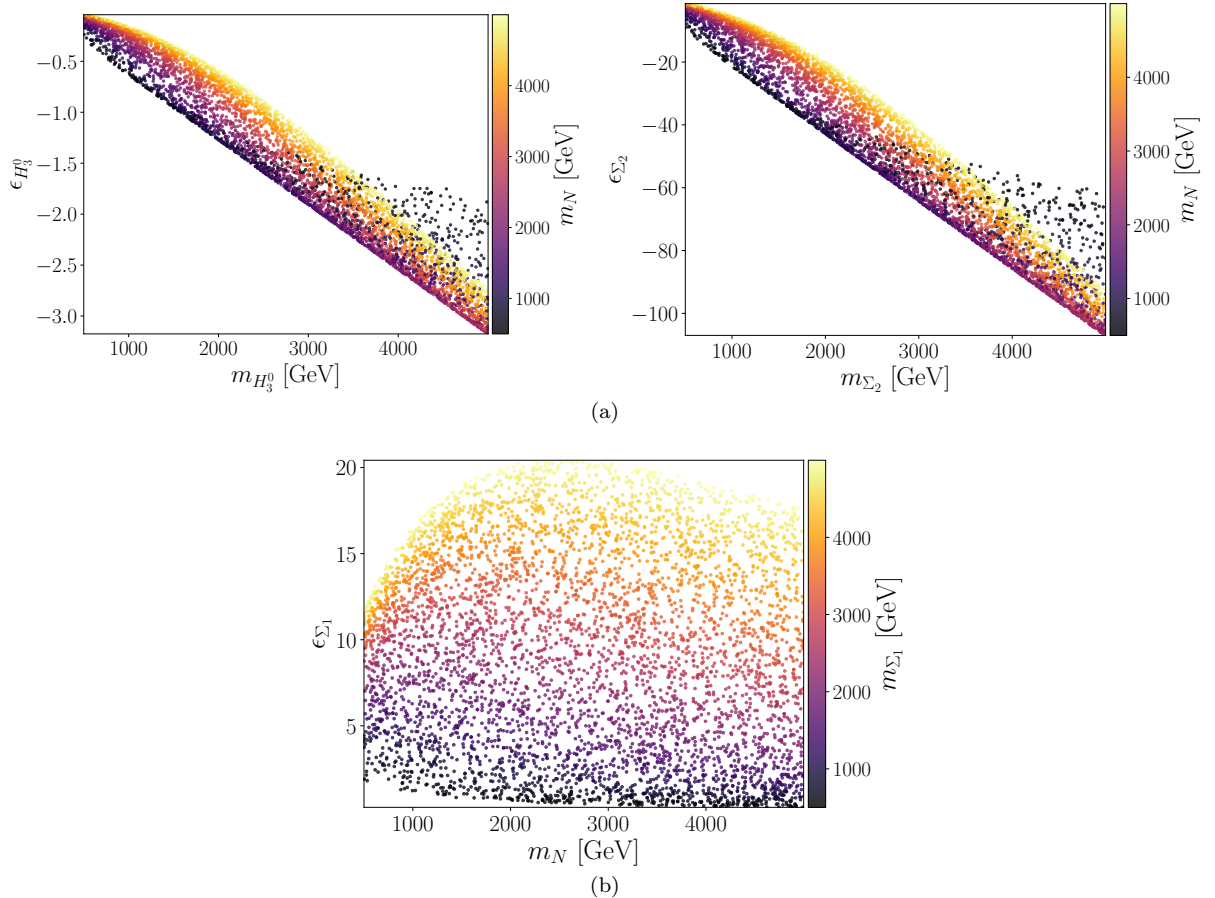


Figure 15: Colour plots of CP asymmetries. In (a) we have the asymmetries of H_3^0 and Σ_2 as function of the masses of the scalars and the heavy neutrino while in (b) we have the asymmetry of Σ_1 as function of the mass of the heavy neutrino.

Since the washout parameters for this model using our benchmark scalar masses are very large we can use their relation to the baryon asymmetry parameter in the strong washout regime [86]

$$Y_{\Delta B} \equiv \frac{n_B - n_{\bar{B}}}{s} = -\frac{28}{79} \frac{0.3 \sum_{\alpha} \epsilon_{S_{\alpha}}}{g_* K_{\text{eff}} (\ln K_{\text{eff}})^{0.6}}. \quad (93)$$

Figure 16 shows a set of values for the baryon asymmetry parameter generated by our model, computed for different values of the Yukawa couplings and the Majorana neutrino mass, which spans in a range from 500 GeV to 5 TeV. The results from the parameter scan demonstrate that our model can successfully reproduce a scenario where the baryon asymmetry parameter falls within the experimental range provided by the PLANCK collaboration [1], thus supporting the feasibility of generating the observed baryon asymmetry via a leptogenesis mechanism.

IX. OBLIQUE PARAMETERS

The oblique parameters play a vital role in the so-called electroweak precision program of the SM due to their high sensitivity to new physics. Many of the observables used as precision tests of the SM are defined at the Z -boson pole, while the W -boson mass provides complementary information about radiative corrections independent of the Z -pole and asymmetries. Consequently, the renormalized propagators of the gauge bosons are highly sensitive to oblique corrections induced by new particles in models BSM.

In our model, the parameters S , T , and U [87–90] receive corrections due to the coupling of exotic scalar particles with the gauge bosons of the SM, modifying the standard corrections. The significance of oblique parameters in BSM models lies in their function as a window to high-energy physics, as heavy exotic particles can induce oblique

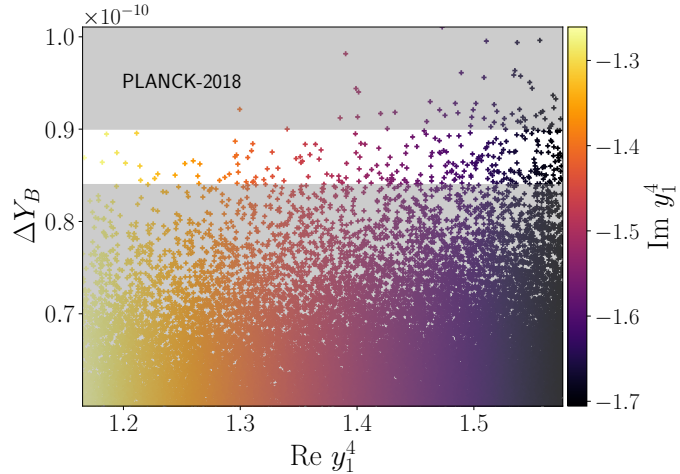


Figure 16: The baryon asymmetry parameter as a function of the real and imaginary parts of the Yukawa coupling y_1^4 . The gray-shaded area denotes the parameter space excluded by the PLANCK collaboration [1].

corrections to the electroweak sector. Due to the stringent constraints on SM extensions, the study of the S , T , and U parameters is a key criterion for assessing the validity of our model.

The oblique parameters S , T , and U are defined in terms of the vacuum polarization tensors $\Pi_{ij}^{\mu\nu}(q^2)$ as:

$$\Pi_{ij}^{\mu\nu}(q^2) = g^{\mu\nu}\Pi_{ij}(q^2) - iq^\mu q^\nu \Delta_{ij}(q^2), \quad (94)$$

where the quantities $\Pi_{ij}(q^2)$ represent the vacuum polarization amplitudes, with $i, j = 0, 1, 3$ corresponding to the B , W_1 , and W_3 gauge bosons, respectively. The effects of new physics can be captured by expanding $\Pi_{ij}(q^2)$ in powers of q^2 , truncated to linear order [89]:

$$\Pi_{ij}(q^2) = \Pi_{ij}(q^2)|_{q^2=0} + q^2 \frac{d}{dq^2} \Pi_{ij}(q^2)|_{q^2=0} + \mathcal{O}(q^4). \quad (95)$$

The oblique corrections, parametrized by the well-known quantities S , T , and U , are defined as follows [88, 89, 91]:

$$\begin{aligned} S &= -\frac{4 \cos \theta_W \sin \theta_W}{\alpha_{\text{em}}} \frac{d}{dq^2} \Pi_{30}(q^2) \Big|_{q^2=0}, \\ U &= \frac{4 \sin \theta_W}{\alpha_{\text{em}}} \frac{d}{dq^2} [\Pi_{11}(q^2) - \Pi_{33}(q^2)] \Big|_{q^2=0}, \\ T &= \frac{1}{\alpha_{\text{em}} M_W^2} [\Pi_{11}(0) - \Pi_{33}(0)] \Big|_{q^2=0}. \end{aligned} \quad (96)$$

where α_{em} is the electromagnetic fine structure constant and θ_W is the Weinberg angle. The calculations for the 2HDM and 3HDM models are extensively discussed in the literature [63, 92], as well as for the generalized case of NHDM [93], which considers a specific scenario where the rotation matrices for pseudoscalars and charged scalars are identical. In our model, as mentioned at the beginning of this section, the new fields associated with Σ , a bidoublet of $SU(2)_2 \times SU(2)_1$, introduce additional couplings to the gauge bosons at the 1-loop level, thereby modifying the

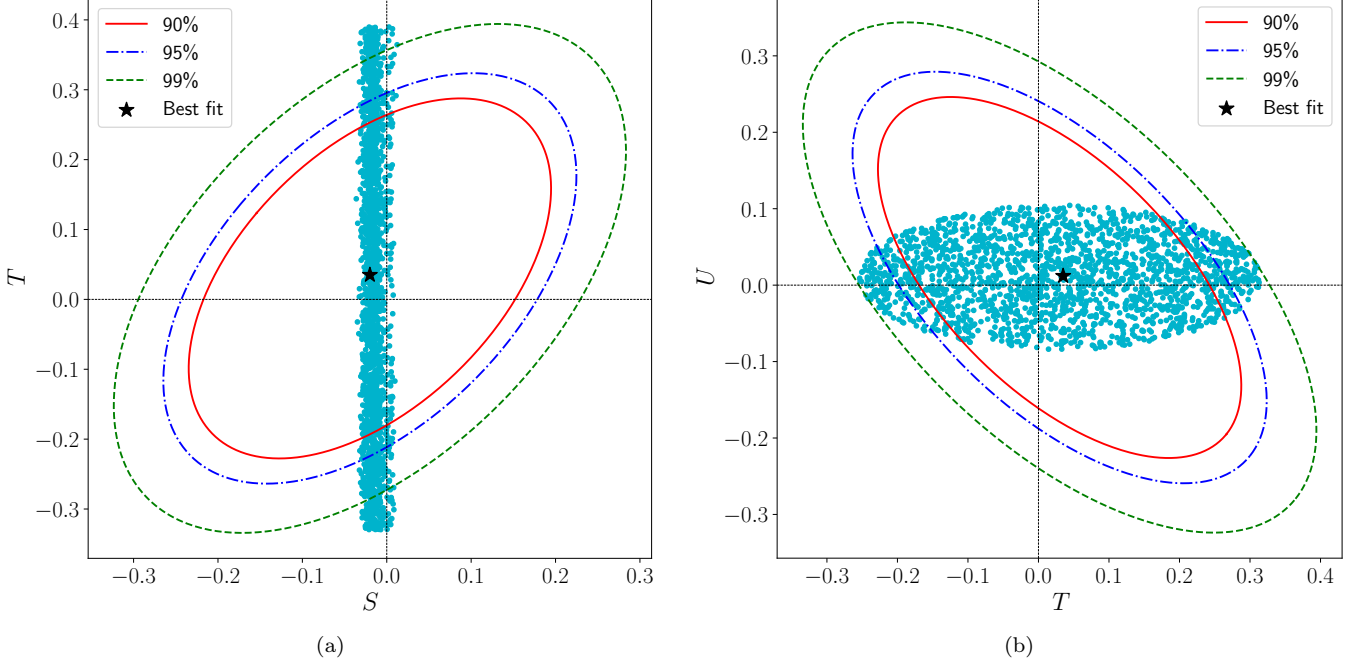


Figure 17: Allowed regions for the oblique parameters in the S - T (left panel) and U - T (right panel) planes. The contours represent confidence levels at 90%, 95%, and 99%, as indicated in the legend. The cyan points correspond to the model predictions, while the black star marks the best fit point, representing the values that minimize the χ^2 function.

values of the oblique parameters. For these computations, we use the expressions derived in [62, 94]

$$S \simeq \frac{1}{12\pi} \sum_{i=1}^3 \sum_{k=1}^2 [(R_H)_{ki} (R_A)_{k1}]^2 K_1 \left(m_{H_i}^2, m_\xi^2, m_{\eta^\pm}^2 \right), \quad (97)$$

$$U \simeq -S + \sum_{a=1}^3 \sum_{k=1}^2 [(R_A)_{a1} (R_C)_{ak}]^2 G_3 (m_\xi, m_{\eta^\pm}) + \sum_{a=1}^3 \sum_{i=1}^3 \sum_{k=1}^2 [(R_H)_{ai} (R_C)_{ak}]^2 G_3 (m_{H_i}, m_{\eta^\pm}), \quad (98)$$

$$T \simeq t_0 \left[\sum_{k=1}^2 m_{\eta^\pm}^2 + \sum_{a=1}^3 \sum_{i=1}^3 [(R_H)_{ai} (R_A)_{a1}]^2 F_3 (m_{H_i}, m_\xi) - \sum_{a=1}^3 \sum_{i=1}^3 \sum_{k=1}^2 [(R_H)_{ai} (R_C)_{ak}]^2 F_3 (m_{H_i}, m_{\eta^\pm}) - \sum_{a=1}^3 \sum_{k=1}^2 [(R_A)_{ai} (R_C)_{ak}]^2 F_3 (m_\xi, m_{\eta^\pm}) \right], \quad (99)$$

where $t_0 = (\pi^2 v_\phi^2 \alpha_{\text{em}} (M_Z))^{-1}$, and R_C , R_H and R_A are the mixing matrices for the charged scalar fields, neutral scalar and pseudoscalars, respectively. Regarding to the masses of the scalar particles H_i they correspond to Σ_1 , Σ_2 and H_3^0 for $i = 1, 2, 3$. Furthermore, the following loop functions were introduced in [92, 93]

$$F_3 (m_1, m_2) = \frac{m_1^2 m_2^2}{m_1^2 - m_2^2} \ln \left(\frac{m_1^2}{m_2^2} \right), \quad (100)$$

$$G_3 (m_1, m_2) = \frac{-5m_1^6 + 27m_1^4 m_2^2 - 27m_1^2 m_2^4 + 6(m_1^6 - 3m_1^4 m_2^2) \ln \left(\frac{m_1^2}{m_2^2} \right) + 5m_2^6}{6(m_1^2 - m_2^2)^3}, \quad (101)$$

$$K_1 (m_1, m_2, m_3) = \frac{1}{(m_2^2 - m_1^2)^3} \left\{ m_1^4 (3m_2^2 - m_1^2) \ln \left(\frac{m_1^2}{m_3^2} \right) - m_2^4 (3m_1^2 - m_2^2) \ln \left(\frac{m_2^2}{m_3^2} \right) - \frac{1}{6} [27m_1^2 m_2^2 (m_1^2 - m_2^2) + 5(m_2^6 - m_1^6)] \right\}. \quad (102)$$

In the numerical analysis, Figure 17 displays the allowed regions in the oblique parameter spaces S - T (left panel) and U - T (right panel) at different confidence levels. The contours represent the 90%, 95%, and 99% confidence levels, as indicated in the legend, and the cyan points correspond to the predictions of our model. These predictions include the contributions of the scalar bidoublet fields and their mixing effects, which play a critical role in modifying the vacuum polarization functions Π_{ij} that define the oblique parameters S , T , and U .

The black star in both panels marks the best-fit point obtained from our model, corresponding to $S = -0.0200 \pm 0.0001$, $T = 0.035 \pm 0.007$, and $U = 0.012 \pm 0.003$, with a χ^2 value of 6.9×10^{-3} . This best-fit point is consistent with the current experimental limits reported in Ref. [46], which are $S_{\text{exp}} = -0.02 \pm 0.1$, $T_{\text{exp}} = 0.03 \pm 0.12$, and $U_{\text{exp}} = 0.01 \pm 0.11$. Notably, the best-fit values lie within 3σ of the experimental bounds, demonstrating that the proposed model aligns well with existing experimental constraints.

In summary, the analysis of the oblique parameters S , T , and U shows that the proposed model is consistent with current experimental limits, highlighting its viability as an extension of the SM. The results, particularly the best-fit point, emphasize the capability of the model's scalar sector to reproduce electroweak precision observables. Moreover, the contributions of the exotic scalar fields and their mixing effects provide a coherent and predictive explanation for deviations in electroweak precision measurements.

X. A POSSIBLE INTERPRETATION OF THE 95 GEV DIPHOTON EXCESS

The CMS collaboration has recently reported an excess of events around 95 GeV in the diphoton invariant mass spectrum, with a local significance approaching 3σ [95, 96]. This intriguing anomaly, if confirmed, would suggest the existence of a new neutral scalar boson lighter than the 125 GeV Higgs. Phenomenologically, such a signal would be highly relevant, representing the first direct evidence of an extended Higgs sector. Several theoretical frameworks—such as Left-Right symmetric models [97, 98] and Two-Higgs-Doublet Models [99–102]—have been proposed to explain this signal. Consequently, it is essential to examine whether our strongly coupled iHDM can naturally reproduce the observed 95 GeV diphoton excess. In our model, there is an attractive candidate for this new state. Out of our benchmark scenario, we can identify the neutral scalar H_3^0 as the resonance responsible for the signal reported by CMS. It is worth mentioning that the scalar potential of our model has a good amount of parametric freedom that allows to successfully accommodate a physical CP even scalar with a mass of 95 GeV. We denote the CP even scalar state responsible for the 95 GeV diphoton excess, as H_{95} , reflecting its mass. In the following analysis, we will demonstrate that the H_{95} state in the our model can indeed produce a diphoton signal of the observed magnitude without conflicting with current experimental constraints.

To quantify the diphoton signal of H_{95} , we define the signal strength in the $\gamma\gamma$ channel as the ratio between the production cross section times the decay branching fraction and that of a SM-like Higgs boson taken as reference. Specifically, focusing on gluon fusion production and the diphoton decay channel, we have

$$\mu(H_{95})_{\gamma\gamma} = \frac{\sigma(gg \rightarrow H_{95})}{\sigma_{\text{SM}}(gg \rightarrow h)} \times \frac{\text{Br}(H_{95} \rightarrow \gamma\gamma)}{\text{Br}(h \rightarrow \gamma\gamma)}, \quad (103)$$

where $\sigma(gg \rightarrow H_{95})$ is the production cross section of the 95 GeV scalar via gluon fusion, $\text{Br}(H_{95} \rightarrow \gamma\gamma)$ is its diphoton branching fraction, and the denominator corresponds to SM values for the Higgs boson.

The experimental measurement for the signal strength of the observed excess at 95 GeV reported by CMS is [96, 103]:

$$\mu_{\gamma\gamma}^{\text{exp}} = 0.35 \pm 0.12. \quad (104)$$

Unlike the Standard Model, where the process $h \rightarrow \gamma\gamma$ receives loop contributions from W^\pm gauge bosons and the top quark, in our model the scalar H_{95} does not possess these tree-level couplings. Nevertheless, it can decay into two photons via loop contributions involving new particles. One of the dominant contributions arises from the vector-like sector; specifically, the model includes heavy quarks T_n ($n = 1, 2$), B_i , and heavy leptons E_i ($i = 1, 2, 3$), which couple to the scalar field associated with σ through Yukawa operators shown in Eq. (9). The corresponding loop contribution is analogous to the one arising from the top-quark loop in the SM Higgs decay into two photons, i.e., it is proportional to the squared electric charge of the fermion Q_f^2 and the Yukawa couplings y_{T_n} , y_{B_i} and y_{E_i} ($\sim M_f/v_\sigma$). In the strongly coupled regime or for small values of v_σ , these loop contributions become positive and significant. Another significant contribution originates from loop effects arising from the extended scalar sector, involving the virtual exchange of the electrically charged scalar fields η^\pm . The spontaneous symmetry breaking yields the trilinear scalar coupling $C_{\sigma\eta^\pm\eta^\mp}$, then giving rise to an interaction of the form $H_{95}\eta^+\eta^-$, whose corresponding coupling can

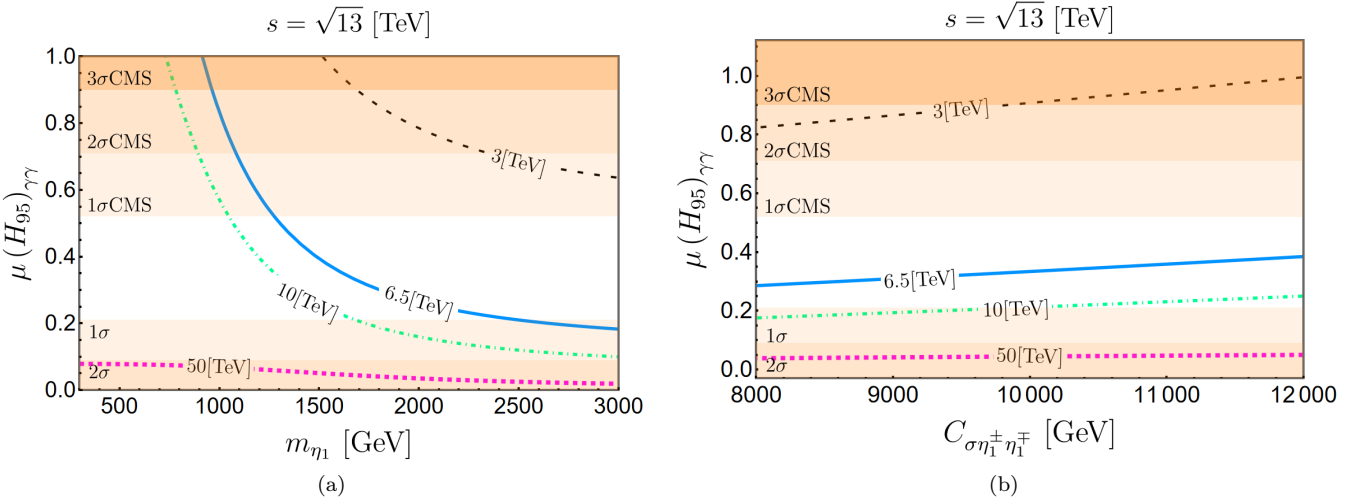


Figure 18: Predictions for the H_{95} boson signal in the $\gamma\gamma$ channel. The signal strength $\mu(H_{95})_{\gamma\gamma}$ is shown as a function of (a) the mass m_{η_1} and (b) the coupling coefficient $C_{\sigma\eta_1^\pm\eta_1^\mp}$. The shaded orange bands represent the exclusion regions at 1σ , 2σ , and 3σ from the CMS analysis. The values indicated on each curve correspond to signal predictions for different values of v_σ .

be expressed as:

$$C_{\sigma\eta_1^\pm\eta_1^\mp} = \left. \frac{\partial^3 V_{\text{Phys}}}{\partial\sigma\partial\eta_1^\pm\partial\eta_1^\mp} \right|_{\text{Fields}=0}, \quad k = 1, 2. \quad (105)$$

The magnitude of this contribution to the 95 GeV diphoton signal is inversely proportional to the square of the masses of the charged scalar fields and directly proportional to the aforementioned trilinear scalar coupling. It is important to note that the scalar loops carry an opposite sign compared to the fermionic loops, provided that the trilinear scalar coupling is positive then implying that in this case their net effect strongly depends on the model parameters. In Refs [98, 104], detailed expressions are provided for the cross section of the diphoton scalar resonance production, as well as for the corresponding decay widths of the resonance into photon and gluon pairs, within BSM theories containing contributions from an extended scalar and exotic charged vector-like fermion sectors.

Figure 18 summarizes the behavior of the signal strength $\mu(H_{95})_{\gamma\gamma}$ as a function of the charged scalar mass m_{η_1} and the effective coupling $H_{95}\eta_1^+\eta_1^-$. The shaded orange bands indicate the experimental 1σ , 2σ , and 3σ regions reported by the CMS collaboration for the mass window around 95 GeV. Figure 18(a) illustrates that, for most of the viable parameter space, the charged scalar loop interferes constructively with fermionic loops, enhancing the branching ratio $\text{Br}(H_{95} \rightarrow \gamma\gamma)$. However, the scalar loop effect rapidly decreases as the scalar mass increases. Additionally, the impact of v_σ shows that for smaller values around 3–4 TeV, significantly larger values of $\mu_{\gamma\gamma}$ are obtained compared to the range of 6–10 TeV for the same scalar mass. Within this latter range, there exists a favorable parameter space consistent with the CMS 1σ region. Meanwhile, the lower curve (corresponding to larger v_σ values) remains below $\mu_{\gamma\gamma} \sim 0.2$, within the 2σ regime, indicating that the model would yield a low signal strength in the weak coupling regime. Overall, this figure highlights a substantial parameter region for moderately low masses of the scalar η_1^\pm and v_σ values consistent with the 95 GeV excess. The curves in Figure 18(b) corroborate the parameter-space scenario described in Figure 18(a). We observe that the signal strength increases monotonically with the trilinear scalar coupling $C_{\sigma\eta_1^\pm\eta_1^\mp}$. A larger coupling implies a greater scalar-loop contribution to the amplitude of $H_{95} \rightarrow \gamma\gamma$, thus enhancing the decay branching fraction. If the trilinear interaction is weak, the signal contribution remains small, with the lower baseline arising from fermionic loops. In our model, it is quite natural to have a moderately large trilinear coupling; hence, achieving the required $\mu_{\gamma\gamma}$ does not constitute a stringent condition, but rather represents a generic possibility within the strongly coupling regime. Consequently, the viable parameter space for obtaining a significant diphoton signal is reinforced.

For the numerical calculations shown in Figure 18, we use a center-of-mass energy of $\sqrt{s} = 13$ TeV, corresponding to the LHC conditions. In the factorization process, we adopt the scale $\mu = m_{H_{95}}$, and for the total cross section we employ the MSTW next-to-leading-order (NLO) gluon distribution functions [105], together with the running strong coupling constant $\alpha_s(M_Z) = 0.1179 \pm 0.0010$.

Figure 19 provides a broader perspective by depicting regions of the vector-like Yukawa coupling space that yield a

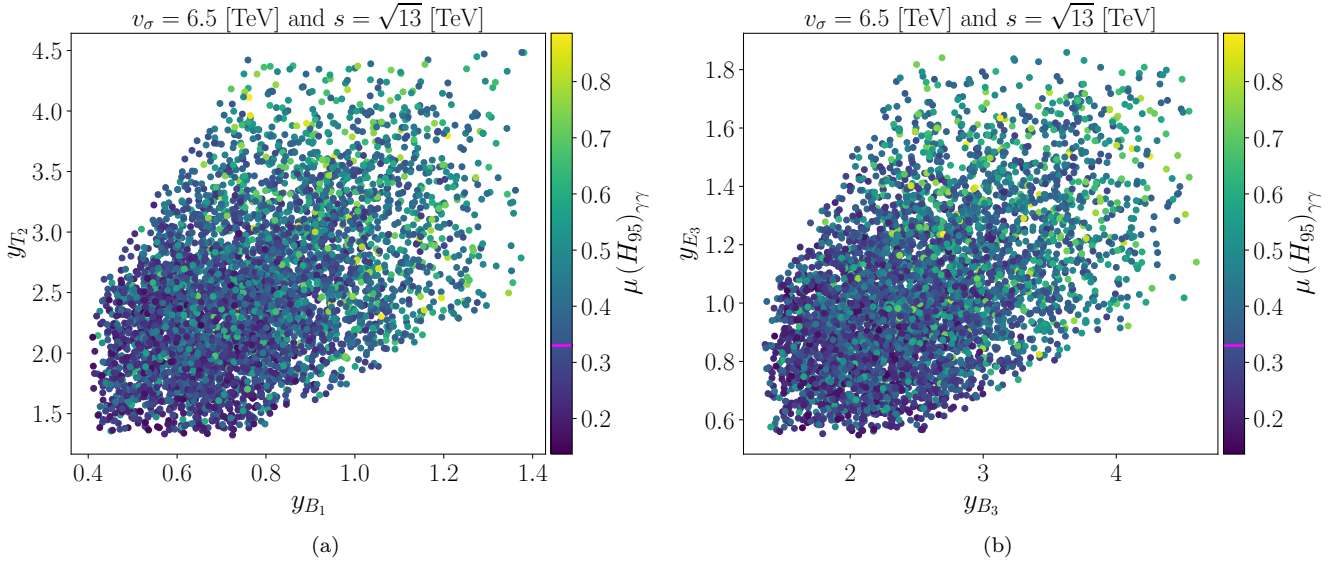


Figure 19: Signal strength $\mu(H_{95})_{\gamma\gamma}$ in the parameter space of the vector-like Yukawa couplings. Panel (a) shows the plane of Yukawa couplings y_{B_1} versus y_{T_2} , while panel (b) displays the plane y_{B_3} versus y_{E_3} . The color bars indicate the magnitude of $\mu(H_{95})_{\gamma\gamma}$, and the horizontal magenta line represents the central value of the CMS measurement at 95 GeV.

given $\mu(H_{95})_{\gamma\gamma}$. Figure 19(a) shows the y_{B_1} versus y_{T_2} plane consistent with the observed $\mu_{\gamma\gamma}$, where the horizontal magenta line on the color bar corresponds to the central CMS measurement value given by Eq. (104). Similarly, Figure 19(b) presents the y_{B_3} versus y_{E_3} plane, with the color bar indicating $\mu(H_{95})_{\gamma\gamma}$ as before. Viable regions for $\mu_{\gamma\gamma}$ in both panels correspond to Yukawa coupling values in the range of 1–3, comfortably within the perturbative regime. Thus, our model can accommodate the large loop contributions required without entering a non-perturbative dynamic regime.

In summary, our model provides a viable interpretation for the 95 GeV diphoton excess without resorting to excessively large couplings or conveniently chosen bound states. The interaction naturally arises through the interplay between the VEV of σ and the masses of the vector-like fermions. This explanation is consistent with the current experimental data and simultaneously leads to a significant set of predictions for future studies.

XI. SUMMARY AND CONCLUSIONS

We have constructed an extension of the SM based on the gauge structure $SU(2)_2 \times SU(2)_1 \times U(1)_Y$, incorporating a strongly coupled inert scalar sector and discrete symmetries. The scalar sector includes two inert Higgs doublets, the SM Higgs doublet, a bidoublet from the $SU(2)_2 \times SU(2)_1$ sector, and a real scalar singlet responsible for the discrete symmetry breaking. This framework successfully addresses key issues such as the hierarchy problem and provides exotic composite states, including massive vector resonances. A novel feature of the model is the inclusion of the exotic scalars in the radiative generation of neutrino masses and universal seesaw mechanisms to yield the masses of the SM charged fermions lighter than the top quark, effectively resolving the SM fermion puzzle. The model successfully reproduces the mass spectra and mixing parameters of quarks and leptons within experimental uncertainties as can be seen in Sec. IV.

The study of the trilinear Higgs self-coupling reveals significant deviations from the SM expectation. The interplay between the extended scalar sector introduces sizeable radiative corrections to the Higgs potential, leading to observable modifications to the trilinear self-coupling of the SM-Higgs. Our work indicates that, despite these corrections, the model remains consistent with current experimental constraints as can be seen in Figure 8. Moreover, the parameter space allows for predictions that can be probed in upcoming collider experiments, particularly through precision measurements of the SM-Higgs self-coupling. This provides a crucial test of the underlying strong dynamics and its potential role in electroweak symmetry breaking.

The model predicts significant contributions to the Higgs diphoton decay rate, $\Gamma_{h \rightarrow \gamma\gamma}$, arising from the one loop level exchange of charged scalars and heavy vector resonances. These contributions modify the decay amplitude through

new quantum corrections, resulting in measurable deviations from the SM predictions. The computed Higgs diphoton signal strength $R_{\gamma\gamma}$ helps to constrain the scalar sector parameter space and aligns well with experimental values as is shown in Table III. Additionally, this observable is stable against variations of the effective β parameter associated with the internal dynamics of the strong sector.

Furthermore, LFV processes, such as $\mu \rightarrow e\gamma$, $\mu \rightarrow 3e$, and $\mu - e$ conversion in a nucleai, are naturally induced at one loop level by interactions among inert scalar doublets, the bidoublet, and heavy neutrinos. Exploring the involved particle masses yields branching ratios within the reach of current and future experiments as indicated in Figure 13, thus providing robust tests for the model.

Our model provides a viable leptogenesis mechanism that exploits the interactions between exotic scalars and heavy neutrinos to generate a leptonic asymmetry in the early Universe. Notably, the partial dominant contribution to the CP asymmetry arises from the decay of the Σ_2 scalar, which plays a crucial role in lepton number violation through its interactions with heavy Majorana neutrinos in out-of-equilibrium decay processes.

The analysis of the baryon asymmetry evolution in the strong washout regime indicates that the baryon asymmetry parameter, ΔY_B , can attain values consistent with the Planck collaboration measurements. This result demonstrates that our model successfully accounts for the origin of the observed matter-antimatter asymmetry in the Universe via a leptogenesis process.

Contributions to the oblique S , T , and U parameters from the extended scalar sector are consistent with experimental constraints. Mixing effects among bidoublet components introduce distinctive modifications, further reinforcing the viability of the model.

The model can naturally accommodate the diphoton excess at 95 GeV reported by CMS, through the interplay of large scalar couplings and the interaction between the scalar singlet σ and the vector-like fermions responsible for the universal seesaw mechanism. One of the exotic scalars in the spectrum can be used to reproduce the observed excess within current experimental bounds.

This model provides a unified framework addressing critical issues in modern particle physics, linking scalar sector extensions to neutrino masses, LFV processes, and precision measurements of the Higgs and electroweak sectors. Predicted deviations in scalar and fermionic observables, influenced by new charged scalars and vector resonances, stand out as distinctive features, offering testable benchmarks for next-generation experiments.

Future efforts should explore other observables, such as

gravitational wave signals. The consistency of the model with current data and novel predictions underscores its relevance as a strong candidate for BSM physics.

Acknowledgments

The authors sincerely thank M. Mora-Urrutia for her contributions during the early stages of the project and for her participation in discussions. D.S.A gratefully acknowledges M. Solis Miquio for his assistance with Python. This research was supported by ANID-Chile under grants PIA/APOYO AFB230003, FONDECYT 1210131, FONDECYT 1210378, FONDECYT 1241855, and Millennium Nucleus Program grant ICN2019_044.

Appendix A: The full scalar potential

For our model, the full scalar potential can be written as

$$V_{\text{full}} = V + \frac{1}{\Lambda^2} V_6 \quad (\text{A1})$$

where V to correpond Eq. (13) and V_6 is the six dimensional non-renormalizable potential, given by

$$\begin{aligned}
V_6 = & \alpha_1 |\phi^\dagger \Sigma h_1|^2 + \alpha_2 |\phi^\dagger \Sigma h_2|^2 + \alpha_3 \left[(\phi^\dagger \Sigma h_1)^2 + (h_1^\dagger \Sigma^\dagger \phi)^2 + \text{H.c.} \right] + \alpha_4 \left[(\phi^\dagger \Sigma h_2)^2 + (h_2^\dagger \Sigma^\dagger \phi)^2 + \text{H.c.} \right] \\
& + \alpha_5 (\phi \phi^\dagger)^3 + \alpha_6 (\phi \phi^\dagger)^2 (h_1 h_1^\dagger) + \alpha_7 (\phi \phi^\dagger)^2 (h_2 h_2^\dagger) + \alpha_8 (\phi \phi^\dagger)^2 (h_1 h_2^\dagger + \text{H.c.}) + \alpha_9 (\phi \phi^\dagger)^2 \text{Tr}(\Sigma \Sigma^\dagger) \\
& + \alpha_{10} (\phi \phi^\dagger)^2 (\sigma \sigma) + \alpha_{11} (\phi \phi^\dagger) (h_1 h_1^\dagger)^2 + \alpha_{12} (\phi \phi^\dagger) \left[(h_1 h_1^\dagger) (h_2 h_2^\dagger) + (h_1 h_2^\dagger + \text{H.c.})^2 \right] \\
& + \alpha_{13} (\phi \phi^\dagger) (h_1 h_1^\dagger) (h_1 h_2^\dagger + \text{H.c.}) + \alpha_{14} (\phi \phi^\dagger) (h_1 h_1^\dagger) \text{Tr}(\Sigma \Sigma^\dagger) + \alpha_{15} (\phi \phi^\dagger) (h_1 h_1^\dagger) (\sigma \sigma) \\
& + \alpha_{16} (\phi \phi^\dagger) (h_2 h_2^\dagger)^2 + \alpha_{17} (\phi \phi^\dagger) (h_2 h_2^\dagger) (h_1 h_2^\dagger + \text{H.c.}) + \alpha_{18} (\phi \phi^\dagger) (h_2 h_2^\dagger) \text{Tr}(\Sigma \Sigma^\dagger) \\
& + \alpha_{19} (\phi \phi^\dagger) (h_2 h_2^\dagger) (\sigma \sigma) + \alpha_{20} (\phi \phi^\dagger) (h_1 h_2^\dagger + \text{H.c.}) \text{Tr}(\Sigma \Sigma^\dagger) + \alpha_{21} (\phi \phi^\dagger) (h_1 h_2^\dagger + \text{H.c.}) (\sigma \sigma) \\
& + \alpha_{22} (\phi \phi^\dagger) \text{Tr}(\Sigma \Sigma^\dagger)^2 + \alpha_{23} (\phi \phi^\dagger) \text{Tr}(\Sigma \Sigma^\dagger) (\sigma \sigma) + \alpha_{24} (\phi \phi^\dagger) (\sigma \sigma)^2 + \alpha_{25} (h_1 h_1^\dagger)^3 + \alpha_{26} (h_1 h_1^\dagger)^2 (\sigma \sigma) \\
& + \alpha_{27} (h_1 h_1^\dagger) \left[(h_1 h_1^\dagger) (h_2 h_2^\dagger) + (h_1 h_2^\dagger + \text{H.c.})^2 \right] + \alpha_{28} (h_1 h_1^\dagger)^2 (h_1 h_2^\dagger + \text{H.c.}) + \alpha_{29} (\sigma \sigma)^3 \\
& + \alpha_{30} \left[(h_1 h_1^\dagger) (h_2 h_2^\dagger) + (h_1 h_2^\dagger + \text{H.c.})^2 \right] (h_2 h_2^\dagger) + \alpha_{31} (h_1 h_1^\dagger) (h_1 h_2^\dagger + \text{H.c.}) \text{Tr}(\Sigma \Sigma^\dagger) \\
& + \alpha_{32} \left[(h_1 h_1^\dagger) (h_2 h_2^\dagger) + (h_1 h_2^\dagger + \text{H.c.})^2 \right] (h_1 h_2^\dagger + \text{H.c.}) + \alpha_{33} (h_1 h_1^\dagger) \text{Tr}(\Sigma \Sigma^\dagger)^2 + \alpha_{34} \text{Tr}(\Sigma \Sigma^\dagger)^3 \\
& + \alpha_{35} \left[(h_1 h_1^\dagger) (h_2 h_2^\dagger) + (h_1 h_2^\dagger + \text{H.c.})^2 \right] \text{Tr}(\Sigma \Sigma^\dagger) + \alpha_{36} \left[(h_1 h_1^\dagger) (h_2 h_2^\dagger) + (h_1 h_2^\dagger + \text{H.c.})^2 \right] (\sigma \sigma) \\
& + \alpha_{37} (h_1 h_1^\dagger) (h_1 h_2^\dagger + \text{H.c.}) (\sigma \sigma) + \alpha_{38} (h_1 h_1^\dagger)^2 \text{Tr}(\Sigma \Sigma^\dagger) + \alpha_{39} (h_2 h_2^\dagger)^2 (h_1 h_2^\dagger + \text{H.c.}) \\
& + \alpha_{40} (h_1 h_1^\dagger) \text{Tr}(\Sigma \Sigma^\dagger) (\sigma \sigma) + \alpha_{41} (h_1 h_1^\dagger) (\sigma \sigma)^2 + \alpha_{42} (h_2 h_2^\dagger)^3 + \alpha_{43} (h_2 h_2^\dagger)^2 \text{Tr}(\Sigma \Sigma^\dagger) \\
& + \alpha_{44} (h_2 h_2^\dagger)^2 (\sigma \sigma) + \alpha_{45} (h_2 h_2^\dagger) (h_1 h_2^\dagger + \text{H.c.}) \text{Tr}(\Sigma \Sigma^\dagger) + \alpha_{46} (h_2 h_2^\dagger) (h_1 h_2^\dagger + \text{H.c.}) (\sigma \sigma) \\
& + \alpha_{47} (h_2 h_2^\dagger) \text{Tr}(\Sigma \Sigma^\dagger)^2 + \alpha_{48} (h_2 h_2^\dagger) \text{Tr}(\Sigma \Sigma^\dagger) (\sigma \sigma) + \alpha_{49} (h_2 h_2^\dagger) (\sigma \sigma)^2 + \alpha_{50} \text{Tr}(\Sigma \Sigma^\dagger)^2 (\sigma \sigma) \\
& + \alpha_{51} (h_1 h_2^\dagger + \text{H.c.}) \text{Tr}(\Sigma \Sigma^\dagger)^2 + \alpha_{52} (h_1 h_2^\dagger + \text{H.c.}) \text{Tr}(\Sigma \Sigma^\dagger) (\sigma \sigma) + \alpha_{53} (h_1 h_2^\dagger + \text{H.c.}) (\sigma \sigma)^2 \\
& + \alpha_{54} \text{Tr}(\Sigma \Sigma^\dagger) (\sigma \sigma)^2
\end{aligned} \tag{A2}$$

Appendix B: The full expressions for gauge boson masses

The full expressions for the gauge boson masses given in Eq.(24) are

$$\begin{aligned}
M_A^2 &= 0, \\
M_Z^2 &= \frac{1}{8} \left((1 + c^2) g_1^2 + c^2 g_2^2 + g_y^2 - \sqrt{(1 + c^2)^2 g_1^4 + 2(-1 + c^2) g_1^2 (c^2 g_2^2 - g_y^2) + (-c^2 g_2^2 + g_y^2)^2} \right) v_\phi^2, \\
M_{\rho_0}^2 &= \frac{1}{8} \left((1 + c^2) g_1^2 + c^2 g_2^2 + g_y^2 + \sqrt{(1 + c^2)^2 g_1^4 + 2(-1 + c^2) g_1^2 (c^2 g_2^2 - g_y^2) + (-c^2 g_2^2 + g_y^2)^2} \right) v_\phi^2, \\
M_{W^\pm}^2 &= \frac{1}{8} \left((1 + c^2) g_1^2 + c^2 g_2^2 - \sqrt{(1 + c^2)^2 g_1^4 + 2c^2 (-1 + c^2) g_1^2 g_2^2 + c^4 g_2^4} \right) v_\phi^2, \\
M_{\rho^\pm}^2 &= \frac{1}{8} \left((1 + c^2) g_1^2 + c^2 g_2^2 + \sqrt{(1 + c^2)^2 g_1^4 + 2c^2 (-1 + c^2) g_1^2 g_2^2 + c^4 g_2^4} \right) v_\phi^2.
\end{aligned} \tag{B1}$$

Appendix C: The effective trilinear higgs coupling

The contribution of the Feynman diagrams in Figure 7 using dimensional regularization is:

$$\begin{aligned} \Gamma_{h^3}^{1\text{-loop}}(q^2) = & \frac{1}{16\pi^2} C_{hHH}^3 C_0(m_h^2, m_h^2, q^2, m_H^2, m_H^2, m_H^2) + \frac{1}{32\pi^2} C_{hHH} C_{hhHH} [B_0(q^2, m_H^2, m_H^2) + 2B_0(m_h^2, m_H^2, m_H^2)] \\ & + \frac{1}{16\pi^2} C_{hAA}^3 C_0(m_h^2, m_h^2, q^2, m_A^2, m_A^2, m_A^2) + \frac{1}{8\pi^2} C_{hCC}^3 C_0(m_h^2, m_h^2, q^2, m_C^2, m_C^2, m_C^2) \\ & + \frac{1}{32\pi^2} C_{hAA} C_{hhAA} [B_0(q^2, m_A^2, m_A^2) + 2B_0(m_h^2, m_A^2, m_A^2)] \\ & + \frac{1}{16\pi^2} C_{hCC} C_{hhCC} [B_0(q^2, m_C^2, m_C^2) + 2B_0(m_h^2, m_C^2, m_C^2)], \end{aligned} \quad (\text{C1})$$

where H , A and C are scalar, pseudoscalar and charged-scalar particles respectively and the functions C_0 and B_0 are the Pasarino-Veltman functions [106–108].

[1] **Planck** Collaboration, N. Aghanim *et al.*, “Planck 2018 results. VI. Cosmological parameters,” *Astron. Astrophys.* **641** (2020) A6, [arXiv:1807.06209 \[astro-ph.CO\]](https://arxiv.org/abs/1807.06209). [Erratum: Astron. Astrophys. 652, C4 (2021)].

[2] B. D. Fields, K. A. Olive, T.-H. Yeh, and C. Young, “Big-Bang Nucleosynthesis after Planck,” *JCAP* **03** (2020) 010, [arXiv:1912.01132 \[astro-ph.CO\]](https://arxiv.org/abs/1912.01132). [Erratum: JCAP 11, E02 (2020)].

[3] **Super-Kamiokande** Collaboration, Y. Fukuda *et al.*, “Evidence for oscillation of atmospheric neutrinos,” *Phys. Rev. Lett.* **81** (1998) 1562–1567, [arXiv:hep-ex/9807003](https://arxiv.org/abs/hep-ex/9807003).

[4] **SNO** Collaboration, Q. R. Ahmad *et al.*, “Measurement of the rate of $\nu_e + d \rightarrow p + p + e^-$ interactions produced by ${}^8\text{B}$ solar neutrinos at the Sudbury Neutrino Observatory,” *Phys. Rev. Lett.* **87** (2001) 071301, [arXiv:nucl-ex/0106015](https://arxiv.org/abs/nucl-ex/0106015).

[5] S. Weinberg, “Implications of Dynamical Symmetry Breaking,” *Phys. Rev. D* **13** (1976) 974–996. [Addendum: *Phys. Rev. D* 19, 1277–1280 (1979)].

[6] L. Susskind, “Dynamics of Spontaneous Symmetry Breaking in the Weinberg-Salam Theory,” *Phys. Rev. D* **20** (1979) 2619–2625.

[7] E. Gildener, “Gauge Symmetry Hierarchies,” *Phys. Rev. D* **14** (1976) 1667.

[8] M. Yamada, “Gauge hierarchy problem and scalegenesis,” *PoS CORFU2019* (2020) 077, [arXiv:2004.00142 \[hep-ph\]](https://arxiv.org/abs/2004.00142).

[9] R. Contino, “New Physics at the LHC: Strong vs. weak symmetry breaking,” *Nuovo Cim.* **32** (2009) 11–18, [arXiv:0908.3578 \[hep-ph\]](https://arxiv.org/abs/0908.3578).

[10] M. Bando, T. Kugo, S. Uehara, K. Yamawaki, and T. Yanagida, “Is rho Meson a Dynamical Gauge Boson of Hidden Local Symmetry?,” *Phys. Rev. Lett.* **54** (1985) 1215.

[11] M. Bando, T. Kugo, and K. Yamawaki, “Composite Gauge Bosons and ‘Low-energy Theorems’ of Hidden Local Symmetries,” *Prog. Theor. Phys.* **73** (1985) 1541.

[12] M. Bando, T. Kugo, and K. Yamawaki, “On the Vector Mesons as Dynamical Gauge Bosons of Hidden Local Symmetries,” *Nucl. Phys. B* **259** (1985) 493.

[13] M. Bando, T. Fujiwara, and K. Yamawaki, “Generalized Hidden Local Symmetry and the A1 Meson,” *Prog. Theor. Phys.* **79** (1988) 1140.

[14] M. Bando, T. Kugo, and K. Yamawaki, “Nonlinear Realization and Hidden Local Symmetries,” *Phys. Rept.* **164** (1988) 217–314.

[15] R. S. Chivukula, B. Coleppa, S. Di Chiara, E. H. Simmons, H.-J. He, M. Kurachi, and M. Tanabashi, “A Three Site Higgsless Model,” *Phys. Rev. D* **74** (2006) 075011, [arXiv:hep-ph/0607124](https://arxiv.org/abs/hep-ph/0607124).

[16] R. Barbieri, A. E. Carcamo Hernandez, G. Corcella, R. Torre, and E. Trincherini, “Composite Vectors at the Large Hadron Collider,” *JHEP* **03** (2010) 068, [arXiv:0911.1942 \[hep-ph\]](https://arxiv.org/abs/0911.1942).

[17] R. Foadi, M. T. Frandsen, T. A. Ryttov, and F. Sannino, “Minimal Walking Technicolor: Set Up for Collider Physics,” *Phys. Rev. D* **76** (2007) 055005, [arXiv:0706.1696 \[hep-ph\]](https://arxiv.org/abs/0706.1696).

[18] T. A. Ryttov and F. Sannino, “Ultra Minimal Technicolor and its Dark Matter TIMP,” *Phys. Rev. D* **78** (2008) 115010, [arXiv:0809.0713 \[hep-ph\]](https://arxiv.org/abs/0809.0713).

[19] F. Sannino, “Conformal Dynamics for TeV Physics and Cosmology,” *Acta Phys. Polon. B* **40** (2009) 3533–3743, [arXiv:0911.0931 \[hep-ph\]](https://arxiv.org/abs/0911.0931).

[20] A. E. Carcamo Hernandez and R. Torre, “A ‘Composite’ scalar-vector system at the LHC,” *Nucl. Phys. B* **841** (2010) 188–204, [arXiv:1005.3809 \[hep-ph\]](https://arxiv.org/abs/1005.3809).

[21] A. E. Carcamo Hernandez, “Top quark effects in composite vector pair production at the LHC,” *Eur. Phys. J. C* **72** (2012) 2154, [arXiv:1008.1039 \[hep-ph\]](https://arxiv.org/abs/1008.1039).

[22] A. E. Carcamo Hernandez, *Composite Vectors and Scalars in Theories of Electroweak Symmetry Breaking*. PhD thesis, Pisa, Scuola Normale Superiore, 2011. [arXiv:1108.0115 \[hep-ph\]](https://arxiv.org/abs/1108.0115).

[23] R. Foadi, M. T. Frandsen, and F. Sannino, “125 GeV Higgs boson from a not so light technicolor scalar,” *Phys. Rev. D* **87** no. 9, (2013) 095001, [arXiv:1211.1083 \[hep-ph\]](https://arxiv.org/abs/1211.1083).

[24] T. Hapola and F. Sannino, “Composite Higgs to two Photons and Gluons,” *Mod. Phys. Lett. A* **26** (2011) 2313–2322, [arXiv:1102.2920 \[hep-ph\]](https://arxiv.org/abs/1102.2920).

[25] A. Belyaev, M. S. Brown, R. Foadi, and M. T. Frandsen, “The Technicolor Higgs in the Light of LHC Data,” *Phys. Rev. D* **90** (2014) 035012, [arXiv:1309.2097 \[hep-ph\]](https://arxiv.org/abs/1309.2097).

[26] A. E. Carcamo Hernandez, C. O. Dib, and A. R. Zerwekh, “The Effect of Composite Resonances on Higgs decay into two photons,” *Eur. Phys. J. C* **74** (2014) 2822, [arXiv:1304.0286 \[hep-ph\]](https://arxiv.org/abs/1304.0286).

[27] A. E. Cárcamo Hernández, B. Díaz Sáez, C. O. Dib, and A. Zerwekh, “Constraints on vector resonances from a strong Higgs sector,” *Phys. Rev. D* **96** no. 11, (2017) 115027, [arXiv:1707.05195 \[hep-ph\]](https://arxiv.org/abs/1707.05195).

[28] W. A. Bardeen, C. T. Hill, and M. Lindner, “Minimal Dynamical Symmetry Breaking of the Standard Model,” *Phys. Rev. D* **41** (1990) 1647.

[29] L. Lopez Honorez, E. Nezri, J. F. Oliver, and M. H. G. Tytgat, “The Inert Doublet Model: An Archetype for Dark Matter,” *JCAP* **02** (2007) 028, [arXiv:hep-ph/0612275](https://arxiv.org/abs/hep-ph/0612275).

[30] I. P. Ivanov and E. Vdovin, “Classification of finite reparametrization symmetry groups in the three-Higgs-doublet model,” *Eur. Phys. J. C* **73** no. 2, (2013) 2309, [arXiv:1210.6553 \[hep-ph\]](https://arxiv.org/abs/1210.6553).

[31] V. Keus, S. F. King, and S. Moretti, “Three-Higgs-doublet models: symmetries, potentials and Higgs boson masses,” *JHEP* **01** (2014) 052, [arXiv:1310.8253 \[hep-ph\]](https://arxiv.org/abs/1310.8253).

[32] A. Aranda, C. Bonilla, and J. L. Diaz-Cruz, “Three generations of Higgses and the cyclic groups,” *Phys. Lett. B* **717** (2012) 248–251, [arXiv:1204.5558 \[hep-ph\]](https://arxiv.org/abs/1204.5558).

[33] A. Aranda, J. E. Barradas-Guevara, A. Cordero-Cid, F. de Anda, A. Delgado, O. Felix-Beltran, and J. Hernandez-Sanchez, “Flavor Physics constrains on a \mathbb{Z}_5 -3HDM,” [arXiv:1404.7829 \[hep-ph\]](https://arxiv.org/abs/1404.7829).

[34] A. Aranda, D. Hernández-Otero, J. Hernández-Sánchez, V. Keus, S. Moretti, D. Rojas-Ciofalo, and T. Shindou, “ \mathbb{Z}_3 symmetric inert (2+1)-Higgs-doublet model,” *Phys. Rev. D* **103** no. 1, (2021) 015023, [arXiv:1907.12470 \[hep-ph\]](https://arxiv.org/abs/1907.12470).

[35] A. G. Akeroyd, S. Moretti, K. Yagyu, and E. Yildirim, “Light charged Higgs boson scenario in 3-Higgs doublet models,” *Int. J. Mod. Phys. A* **32** no. 23n24, (2017) 1750145, [arXiv:1605.05881 \[hep-ph\]](https://arxiv.org/abs/1605.05881).

[36] A. E. C. Hernández, S. Kovalenko, M. Maniatis, and I. Schmidt, “Fermion mass hierarchy and $g - 2$ anomalies in an extended 3HDM Model,” *JHEP* **10** (2021) 036, [arXiv:2104.07047 \[hep-ph\]](https://arxiv.org/abs/2104.07047).

[37] A. R. Zerwekh, “Two Composite Higgs Doublets: Is it the Low Energy Limit of a Natural Strong Electroweak Symmetry Breaking Sector?,” *Mod. Phys. Lett. A* **25** (2010) 423–429, [arXiv:0907.4690 \[hep-ph\]](https://arxiv.org/abs/0907.4690).

[38] S. Di Chiara, M. Heikinheimo, and K. Tuominen, “Vector resonances at LHC Run II in composite 2HDM,” *JHEP* **03** (2017) 009, [arXiv:1611.09094 \[hep-ph\]](https://arxiv.org/abs/1611.09094).

[39] S. De Curtis, S. Moretti, K. Yagyu, and E. Yildirim, “Perturbative unitarity bounds in composite two-Higgs doublet models,” *Phys. Rev. D* **94** no. 5, (2016) 055017, [arXiv:1602.06437 \[hep-ph\]](https://arxiv.org/abs/1602.06437).

[40] F. Rojas-Abatte, M. L. Mora, J. Urbina, and A. R. Zerwekh, “Inert two-Higgs-doublet model strongly coupled to a non-Abelian vector resonance,” *Phys. Rev. D* **96** no. 9, (2017) 095025, [arXiv:1707.04543 \[hep-ph\]](https://arxiv.org/abs/1707.04543).

[41] R. S. Chivukula, E. H. Simmons, B. Coleppa, H. E. Logan, and A. Martin, “Top-Higgs and Top-Pion Phenomenology in the Top Triangle Moose Model,” *Phys. Rev. D* **83** (2011) 055013, [arXiv:1101.6023 \[hep-ph\]](https://arxiv.org/abs/1101.6023).

[42] R. Sekhar Chivukula, N. D. Christensen, B. Coleppa, and E. H. Simmons, “The Top Triangle Moose: Combining Higgsless and Topcolor Mechanisms for Mass Generation,” *Phys. Rev. D* **80** (2009) 035011, [arXiv:0906.5567 \[hep-ph\]](https://arxiv.org/abs/0906.5567).

[43] P. Osland, A. A. Pankov, and I. A. Serenkova, “Updated constraints on Z' and W' bosons decaying into bosonic and leptonic final states using the run 2 ATLAS data,” *Phys. Rev. D* **103** no. 5, (2021) 053009, [arXiv:2012.13930 \[hep-ph\]](https://arxiv.org/abs/2012.13930).

[44] A. A. Pankov, I. A. Serenkova, and V. A. Bednyakov, “Updated Constraints on Heavy Resonances Using the run 2 Data at LHC,” *Odessa Astron. Pub.* **34** (2021) 18–22.

[45] G. Bhattacharyya and D. Das, “Scalar sector of two-Higgs-doublet models: A minireview,” *Pramana* **87** no. 3, (2016) 40, [arXiv:1507.06424 \[hep-ph\]](https://arxiv.org/abs/1507.06424).

[46] **Particle Data Group** Collaboration, R. L. Workman and Others, “Review of Particle Physics,” *PTEP* **2022** (2022) 083C01.

[47] Z.-j. Tao, “Radiative seesaw mechanism at weak scale,” *Phys. Rev. D* **54** (1996) 5693–5697, [arXiv:hep-ph/9603309](https://arxiv.org/abs/hep-ph/9603309).

[48] E. Ma, “Verifiable radiative seesaw mechanism of neutrino mass and dark matter,” *Phys. Rev. D* **73** (2006) 077301, [arXiv:hep-ph/0601225](https://arxiv.org/abs/hep-ph/0601225).

[49] Z.-z. Xing, “Flavor structures of charged fermions and massive neutrinos,” *Phys. Rept.* **854** (2020) 1–147, [arXiv:1909.09610 \[hep-ph\]](https://arxiv.org/abs/1909.09610).

[50] P. F. de Salas, D. V. Forero, S. Gariazzo, P. Martínez-Miravé, O. Mena, C. A. Ternes, M. Tórtola, and J. W. F. Valle, “2020 global reassessment of the neutrino oscillation picture,” *JHEP* **02** (2021) 071, [arXiv:2006.11237 \[hep-ph\]](https://arxiv.org/abs/2006.11237).

[51] J. Alison *et al.*, “Higgs boson potential at colliders: Status and perspectives,” *Rev. Phys.* **5** (2020) 100045, [arXiv:1910.00012 \[hep-ph\]](https://arxiv.org/abs/1910.00012).

[52] H. Abouabid *et al.*, “HHH whitepaper,” *Eur. Phys. J. C* **84** (2024) 1183, [arXiv:2407.03015 \[hep-ph\]](https://arxiv.org/abs/2407.03015).

[53] **ATLAS** Collaboration, G. Aad *et al.*, “Constraints on the Higgs boson self-coupling from single- and double-Higgs production with the ATLAS detector using pp collisions at $s=13$ TeV,” *Phys. Lett. B* **843** (2023) 137745, [arXiv:2211.01216 \[hep-ex\]](https://arxiv.org/abs/2211.01216).

[54] A. Arhrib, R. Benbrik, J. El Falaki, and A. Jueid, “Radiative corrections to the Triple Higgs Coupling in the Inert Higgs Doublet Model,” *JHEP* **12** (2015) 007, [arXiv:1507.03630 \[hep-ph\]](https://arxiv.org/abs/1507.03630).

[55] S. Kanemura, M. Kikuchi, and K. Yagyu, “One-loop corrections to the Higgs self-couplings in the singlet extension,”

Nucl. Phys. B **917** (2017) 154–177, [arXiv:1608.01582 \[hep-ph\]](https://arxiv.org/abs/1608.01582).

[56] A. Moyotl, S. Chamorro, H. Castilla-Valdez, and M. A. Pérez, “New physics effects in the Higgs trilinear self-coupling through one-loop radiative corrections,” [arXiv:1610.06299 \[hep-ph\]](https://arxiv.org/abs/1610.06299).

[57] S. Kanemura, M. Kikuchi, K. Sakurai, and K. Yagyu, “Gauge invariant one-loop corrections to Higgs boson couplings in non-minimal Higgs models,” *Phys. Rev. D* **96** no. 3, (2017) 035014, [arXiv:1705.05399 \[hep-ph\]](https://arxiv.org/abs/1705.05399).

[58] S. Kanemura, Y. Okada, E. Senaha, and C. P. Yuan, “Higgs coupling constants as a probe of new physics,” *Phys. Rev. D* **70** (2004) 115002, [arXiv:hep-ph/0408364](https://arxiv.org/abs/hep-ph/0408364).

[59] S. Kanemura, S. Kiyoura, Y. Okada, E. Senaha, and C. P. Yuan, “New physics effect on the Higgs selfcoupling,” *Phys. Lett. B* **558** (2003) 157–164, [arXiv:hep-ph/0211308](https://arxiv.org/abs/hep-ph/0211308).

[60] G. Bhattacharyya and D. Das, “Nondecoupling of charged scalars in Higgs decay to two photons and symmetries of the scalar potential,” *Phys. Rev. D* **91** (2015) 015005, [arXiv:1408.6133 \[hep-ph\]](https://arxiv.org/abs/1408.6133).

[61] H. E. Logan, “TASI 2013 lectures on Higgs physics within and beyond the Standard Model,” [arXiv:1406.1786 \[hep-ph\]](https://arxiv.org/abs/1406.1786).

[62] A. E. Cárcamo Hernández, J. Marchant González, D. Salinas-Arizmendi, and M. L. Mora-Urrutia, “Phenomenological aspects of the fermion and scalar sectors of a S4 flavored 3-3-1 model,” *Nucl. Phys. B* **1005** (2024) 116588, [arXiv:2305.13441 \[hep-ph\]](https://arxiv.org/abs/2305.13441).

[63] A. E. Cárcamo Hernández, D. Salinas-Arizmendi, J. Vignatti, and A. Zerwekh, “Phenomenology of an Extended 1 + 2 Higgs Doublet Model with S_3 Family Symmetry,” [arXiv:2408.01497 \[hep-ph\]](https://arxiv.org/abs/2408.01497).

[64] ATLAS Collaboration, G. Aad *et al.*, “A detailed map of Higgs boson interactions by the ATLAS experiment ten years after the discovery,” *Nature* **607** no. 7917, (2022) 52–59, [arXiv:2207.00092 \[hep-ex\]](https://arxiv.org/abs/2207.00092). [Erratum: *Nature* 612, E24 (2022)].

[65] ATLAS Collaboration, G. Aad *et al.*, “Measurement of the properties of Higgs boson production at $\sqrt{s} = 13$ TeV in the $H \rightarrow \gamma\gamma$ channel using 139 fb^{-1} of pp collision data with the ATLAS experiment,” *JHEP* **07** (2023) 088, [arXiv:2207.00348 \[hep-ex\]](https://arxiv.org/abs/2207.00348).

[66] CMS Collaboration, P. Saha, “Recent Measurements of Higgs Boson Properties in the Diphoton Decay Channel with the CMS Detector,” *Springer Proc. Phys.* **277** (2022) 183–186.

[67] M. Ardu and G. Pezzullo, “Introduction to Charged Lepton Flavor Violation,” *Universe* **8** no. 6, (2022) 299, [arXiv:2204.08220 \[hep-ph\]](https://arxiv.org/abs/2204.08220).

[68] T. Toma and A. Vicente, “Lepton Flavor Violation in the Scotogenic Model,” *JHEP* **01** (2014) 160, [arXiv:1312.2840 \[hep-ph\]](https://arxiv.org/abs/1312.2840).

[69] A. Vicente and C. E. Yaguna, “Probing the scotogenic model with lepton flavor violating processes,” *JHEP* **02** (2015) 144, [arXiv:1412.2545 \[hep-ph\]](https://arxiv.org/abs/1412.2545).

[70] A. Abada, N. Bernal, A. E. Cárcamo Hernández, S. Kovalenko, T. B. de Melo, and T. Toma, “Phenomenological and cosmological implications of a scotogenic three-loop neutrino mass model,” *JHEP* **03** (2023) 035, [arXiv:2212.06852 \[hep-ph\]](https://arxiv.org/abs/2212.06852).

[71] MEG Collaboration, A. M. Baldini *et al.*, “Search for the lepton flavour violating decay $\mu^+ \rightarrow e^+ \gamma$ with the full dataset of the MEG experiment,” *Eur. Phys. J. C* **76** no. 8, (2016) 434, [arXiv:1605.05081 \[hep-ex\]](https://arxiv.org/abs/1605.05081).

[72] MEG II Collaboration, K. Afanaciev *et al.*, “New limit on the $\mu^+ \rightarrow e^+ \gamma$ decay with the MEG II experiment,” [arXiv:2504.15711 \[hep-ex\]](https://arxiv.org/abs/2504.15711).

[73] M. Lindner, M. Platscher, and F. S. Queiroz, “A Call for New Physics : The Muon Anomalous Magnetic Moment and Lepton Flavor Violation,” *Phys. Rept.* **731** (2018) 1–82, [arXiv:1610.06587 \[hep-ph\]](https://arxiv.org/abs/1610.06587).

[74] H. C. Chiang, E. Oset, T. S. Kosmas, A. Faessler, and J. D. Vergados, “Coherent and incoherent (μ -, e -) conversion in nuclei,” *Nucl. Phys. A* **559** (1993) 526–542.

[75] R. Kitano, M. Koike, and Y. Okada, “Detailed calculation of lepton flavor violating muon electron conversion rate for various nuclei,” *Phys. Rev. D* **66** (2002) 096002, [arXiv:hep-ph/0203110](https://arxiv.org/abs/hep-ph/0203110). [Erratum: *Phys. Rev. D* 76, 059902 (2007)].

[76] T. S. Kosmas, S. Kovalenko, and I. Schmidt, “Nuclear muon- e - conversion in strange quark sea,” *Phys. Lett. B* **511** (2001) 203, [arXiv:hep-ph/0102101](https://arxiv.org/abs/hep-ph/0102101).

[77] SINDRUM Collaboration, U. Bellgardt *et al.*, “Search for the Decay $\mu^+ \rightarrow e^+ e^+ e^-$,” *Nucl. Phys. B* **299** (1988) 1–6.

[78] MEG Collaboration, T. Mori, “Final Results of the MEG Experiment,” *Nuovo Cim. C* **39** no. 4, (2017) 325, [arXiv:1606.08168 \[hep-ex\]](https://arxiv.org/abs/1606.08168).

[79] A. Blondel *et al.*, “Research Proposal for an Experiment to Search for the Decay $\mu \rightarrow eee$,” [arXiv:1301.6113 \[physics.ins-det\]](https://arxiv.org/abs/1301.6113).

[80] P. Wintz, “Results of the SINDRUM-II experiment,” *Conf. Proc. C* **980420** (1998) 534–546.

[81] R. H. Bernstein and P. S. Cooper, “Charged Lepton Flavor Violation: An Experimenter’s Guide,” *Phys. Rept.* **532** (2013) 27–64, [arXiv:1307.5787 \[hep-ex\]](https://arxiv.org/abs/1307.5787).

[82] A. D. Sakharov, “Violation of CP Invariance, C asymmetry, and baryon asymmetry of the universe,” *Pisma Zh. Eksp. Teor. Fiz.* **5** (1967) 32–35.

[83] A. Datta, R. Roshan, and A. Sil, “Scalar triplet flavor leptogenesis with dark matter,” *Phys. Rev. D* **105** no. 9, (2022) 095032, [arXiv:2110.03914 \[hep-ph\]](https://arxiv.org/abs/2110.03914).

[84] T. Hambye, M. Raidal, and A. Strumia, “Efficiency and maximal CP-asymmetry of scalar triplet leptogenesis,” *Phys. Lett. B* **632** (2006) 667–674, [arXiv:hep-ph/0510008](https://arxiv.org/abs/hep-ph/0510008).

[85] W.-B. Lu and P.-H. Gu, “Leptogenesis, radiative neutrino masses and inert Higgs triplet dark matter,” *JCAP* **05** (2016) 040, [arXiv:1603.05074 \[hep-ph\]](https://arxiv.org/abs/1603.05074).

[86] A. Pilaftsis, “CP violation and baryogenesis due to heavy Majorana neutrinos,” *Phys. Rev. D* **56** (1997) 5431–5451,

[arXiv:hep-ph/9707235](https://arxiv.org/abs/hep-ph/9707235).

[87] M. E. Peskin and T. Takeuchi, “A New constraint on a strongly interacting Higgs sector,” *Phys. Rev. Lett.* **65** (1990) 964–967.

[88] G. Altarelli and R. Barbieri, “Vacuum polarization effects of new physics on electroweak processes,” *Phys. Lett. B* **253** (1991) 161–167.

[89] M. E. Peskin and T. Takeuchi, “Estimation of oblique electroweak corrections,” *Phys. Rev. D* **46** (1992) 381–409.

[90] G. Altarelli, R. Barbieri, and S. Jadach, “Toward a model independent analysis of electroweak data,” *Nucl. Phys. B* **369** (1992) 3–32. [Erratum: Nucl.Phys.B 376, 444 (1992)].

[91] R. Barbieri, A. Pomarol, R. Rattazzi, and A. Strumia, “Electroweak symmetry breaking after LEP-1 and LEP-2,” *Nucl. Phys. B* **703** (2004) 127–146, [arXiv:hep-ph/0405040](https://arxiv.org/abs/hep-ph/0405040).

[92] A. E. Cárcamo Hernández, I. de Medeiros Varzielas, and E. Schumacher, “Fermion and scalar phenomenology of a two-Higgs-doublet model with S_3 ,” *Phys. Rev. D* **93** no. 1, (2016) 016003, [arXiv:1509.02083](https://arxiv.org/abs/1509.02083) [hep-ph].

[93] A. E. Cárcamo Hernández, S. Kovalenko, and I. Schmidt, “Precision measurements constraints on the number of Higgs doublets,” *Phys. Rev. D* **91** (2015) 095014, [arXiv:1503.03026](https://arxiv.org/abs/1503.03026) [hep-ph].

[94] W. Grimus, L. Lavoura, O. M. Ogreid, and P. Osland, “The Oblique parameters in multi-Higgs-doublet models,” *Nucl. Phys. B* **801** (2008) 81–96, [arXiv:0802.4353](https://arxiv.org/abs/0802.4353) [hep-ph].

[95] CMS Collaboration, A. M. Sirunyan *et al.*, “Search for a standard model-like Higgs boson in the mass range between 70 and 110 GeV in the diphoton final state in proton-proton collisions at $\sqrt{s} = 8$ and 13 TeV,” *Phys. Lett. B* **793** (2019) 320–347, [arXiv:1811.08459](https://arxiv.org/abs/1811.08459) [hep-ex].

[96] CMS Collaboration, “Search for a standard model-like Higgs boson in the mass range between 70 and 110 GeV in the diphoton final state in proton-proton collisions at $\sqrt{s} = 13$ TeV.”

[97] P. S. B. Dev, R. N. Mohapatra, and Y. Zhang, “Explanation of the 95 GeV $\gamma\gamma$ and bb^- excesses in the minimal left-right symmetric model,” *Phys. Lett. B* **849** (2024) 138481, [arXiv:2312.17733](https://arxiv.org/abs/2312.17733) [hep-ph].

[98] C. Bonilla, A. E. Cárcamo Hernandez, S. Kovalenko, H. Lee, R. Pasechnik, and I. Schmidt, “Fermion mass hierarchy in an extended left-right symmetric model,” *JHEP* **12** (2023) 075, [arXiv:2305.11967](https://arxiv.org/abs/2305.11967) [hep-ph].

[99] B. Ait-Ouazghour, M. Chabab, and K. Goure, “Unified Interpretation of 95 GeV Excesses in the Two Higgs Doublet type II Seesaw Model,” [arXiv:2410.11140](https://arxiv.org/abs/2410.11140) [hep-ph].

[100] P. Sharma, A.-T. Mulaudzi, K. Mosala, T. Mathaha, M. Kumar, B. Mellado, A. Crivellin, M. Titov, M. Ruan, and Y. Fang, “Discovery Potential of Future Electron-Positron Colliders for a 95 GeV Scalar,” [arXiv:2407.16806](https://arxiv.org/abs/2407.16806) [hep-ph].

[101] S. Banik, G. Coloretti, A. Crivellin, and H. E. Haber, “Correlating $A \rightarrow \gamma\gamma$ with electric dipole moments in the two Higgs doublet model in light of the diphoton excesses at 95 GeV and 152 GeV,” *Phys. Rev. D* **111** no. 7, (2025) 075021, [arXiv:2412.00523](https://arxiv.org/abs/2412.00523) [hep-ph].

[102] A. Belyaev, R. Benbrik, M. Boukidi, M. Chakraborti, S. Moretti, and S. Semlali, “Explanation of the hints for a 95 GeV Higgs boson within a 2-Higgs Doublet Model,” *JHEP* **05** (2024) 209, [arXiv:2306.09029](https://arxiv.org/abs/2306.09029) [hep-ph].

[103] T. Biekötter, S. Heinemeyer, and G. Weiglein, “The CMS di-photon excess at 95 GeV in view of the LHC Run 2 results,” *Phys. Lett. B* **846** (2023) 138217, [arXiv:2303.12018](https://arxiv.org/abs/2303.12018) [hep-ph].

[104] D. T. Huong, A. E. Cárcamo Hernández, H. T. Hung, T. T. Hieu, and N. A. Pérez-Julve, “Extended IDM theory with low scale seesaw mechanisms,” [arXiv:2502.19488](https://arxiv.org/abs/2502.19488) [hep-ph].

[105] A. D. Martin, W. J. Stirling, R. S. Thorne, and G. Watt, “Parton distributions for the LHC,” *Eur. Phys. J. C* **63** (2009) 189–285, [arXiv:0901.0002](https://arxiv.org/abs/0901.0002) [hep-ph].

[106] G. ’t Hooft and M. J. G. Veltman, “Regularization and Renormalization of Gauge Fields,” *Nucl. Phys. B* **44** (1972) 189–213.

[107] G. ’t Hooft and M. J. G. Veltman, “Scalar One Loop Integrals,” *Nucl. Phys. B* **153** (1979) 365–401.

[108] G. Passarino and M. J. G. Veltman, “One Loop Corrections for e+ e- Annihilation Into mu+ mu- in the Weinberg Model,” *Nucl. Phys. B* **160** (1979) 151–207.